

A Swift X-Ray View of the SMS4 Sample - X-Ray Properties of 31 Quasars and Radio Galaxies

ALESSANDRO MASELLI ^{1,2} WILLIAM R. FORMAN ³ CHRISTINE JONES ³ RALPH P. KRAFT ³ AND
MATTEO PERRI ^{1,2}

¹*INAF-Osservatorio Astronomico di Roma
via Frascati 33, I-00078, Monte Porzio Catone (Roma), Italy*

²*ASI-Space Science Data Center
via del Politecnico snc, I-00133, Roma, Italy*

³*Harvard-Smithsonian Center for Astrophysics
60 Garden Street, Cambridge, MA 02138, USA*

ABSTRACT

We present Neil Gehrels Swift Observatory (hereafter Swift) observations of 31 sources from the SMS4 catalog, a sample of 137 bright radio sources originally designed to extend the well-studied 3CRR radio sample to the southern hemisphere. All these sources had no Chandra or XMM-Newton observations: 24 of these were observed with Swift through a dedicated proposal in 2015, and data for the remaining seven were retrieved from the Swift archive. The reduction and analysis of data collected by the Swift X-ray Telescope (XRT) led to 20 detections in the 0.3–10 keV band. We provide details of the X-ray emission in this band for these 20 detections, as well as upper limits for the remaining 11 SMS4 sources. When statistics allowed, we investigated the extent of the X-ray emission and the hardness ratio, and we carried out a spectral analysis. We matched the 20 X-ray-detected sources with infrared (AllWISE, CatWISE2020) and optical (GSC 2.3.2, DES DR2) catalogs to establish associations with infrared and optical sources, and compared our results with previously published counterparts in these bands. Requiring a detection in both the infrared and the optical bands to establish a candidate counterpart for our X-ray detections, we obtain reliable counterparts for 18 sources, while the remaining two sources need further investigation to establish firm identifications. In the infrared, we confirm 12 previously established counterparts and provide six new candidates. In the optical, we find agreement with 13 previously established counterparts, while we provide an alternative candidate for five SMS4 sources. We find that $\sim 35\%$ of all the SMS4 sources lie below the lower limit of 10.9 Jy for the flux density at 178 MHz established for the 3CRR sample, at variance with the values extrapolated using measurements at higher frequencies. Therefore, for future studies where flux-density-limited samples are needed, we encourage the use of the more recent G4Jy sample. We present the list of 56 SMS4 sources that in 2022 March remain to be observed in the X-rays with narrow-field instruments, to highlight interesting sources and organize further observational campaigns to achieve complete X-ray coverage for the whole SMS4 in the forthcoming years.

Keywords: Active galaxies (17) — Extragalactic radio sources (508) — X-ray sources (1810)

1. INTRODUCTION

Over the past few decades, observational evidence of the major role played by central supermassive black holes (SMBHs) in the evolution of their host galaxies has progressively increased. The processes by which such an

influence occurs are referred to as active galactic nucleus (AGN) feedback (for a recent review, see [Werner et al. 2019](#)).

In a simplified picture that has gained large consensus, two major feedback modes, controlled by the accretion rate onto the SMBH, have been identified ([Churazov et al. 2005](#)). In the so-called radio - or mechanical - mode, operating at low accretion rates, relativistic outflows from the SMBH would be able to transfer energy to

the surrounding medium, over a wide range of distances (McNamara & Nulsen 2007, 2012).

For brightest cluster galaxies (BCGs) at the center of cooling flows (see Fabian 1994 for a review) these plasma jets would have the remarkable role of balancing the radiative losses of the X-ray-emitting gas in the intracluster medium (Churazov et al. 2002; Bykov et al. 2015), giving a solution to the *cooling flow problem*. More generally, the outflows would also heat the coronae surrounding massive elliptical galaxies (Forman et al. 1985), reducing the star formation rate up to its substantial quenching. Shock fronts and cavities within these hot X-ray atmospheres, associated with the expansion of jet radio lobes, have been revealed through the comparison between detailed radio and X-ray images and have been interpreted in the framework of such interaction (see, *e.g.*, Finoguenov & Jones 2001; Jones et al. 2002; Kraft et al. 2003; Forman et al. 2005, 2007; Randall et al. 2011, 2015).

The need to properly take AGN feedback into account has been assessed also by cosmological simulations, based on a semianalytic approach (see, *e.g.*, Croton et al. 2006, 2016), as well as by hydrodynamical simulations like those from the recent EAGLE (Schaye et al. 2015; Crain et al. 2015) and Illustris (Vogelsberger et al. 2013; Pillepich et al. 2018) projects.

The best way to obtain essential information about the X-ray emission from radio-loud AGNs (*e.g.*, radio galaxies and radio bright quasars) and their environments is to select complete, flux-limited samples from low-frequency radio surveys, which span a wide range in radio power and redshift and also are unbiased with respect to the angle between the jet and our line of sight. So far, despite a rich collection of galaxies investigated in great detail, a consistent number of luminous radio sources remains poorly explored in X-rays using pointed observations with narrow-field instruments.

For the Northern Hemisphere, the Third Cambridge (3C) Catalog (Edge et al. 1959), along its revisions, the 3CR (Bennett 1962) and the 3CRR (Laing et al. 1983), is a premier sample for understanding the nature and evolution of powerful radio galaxies, as well as their relationship to their host galaxies and environments, on scales from parsecs to megaparsecs. The 3CRR sample was built from a survey at 178 MHz carried out with the Cambridge interferometer and includes 173 sources at $\delta \geq 10^\circ$, at $|b| \geq 10^\circ$, and with a flux density S_{178} higher than $S_{178}^* = 10.9$ Jy.

In 2006, with the goal of expanding the 3CRR catalog into the Southern Hemisphere, a sample of extremely bright radio sources (Burgess & Hunstead 2006a) was extracted from the Molonglo Reference Cat-

alogue (MRC; Large et al. 1981, 1991), based on a low-frequency survey at 408 MHz. The first step was the compilation of the Molonglo Southern 4 Jy (MS4) sample, which included 228 sources at $-30^\circ \leq \delta \leq -85^\circ$, at $|b| > 10^\circ$, and with $S_{408} > 4.0$ Jy. These 228 sources were all imaged at 843 MHz with the Molonglo Observatory Synthesis Telescope (MOST) to establish accurate positions, flux densities, and angular sizes. Then, the 133 MS4 sources with largest angular size (LAS) $< 35''$ were selected for high-resolution imaging at 5 GHz with the Australia Telescope Compact Array (ATCA). Optical identification for all MS4 sources was pursued complementing the analysis on plates from the UK Schmidt Southern Sky Survey with *R*-band CCD images made with the Anglo-Australian Telescope (AAT) (Burgess & Hunstead 2006b). Furthermore, spectral information at other frequencies was collected from the literature to derive S_{178} for all MS4 sources. Hence, by using the same flux density threshold S_{178}^* as in the 3CRR catalog, a strong-source subset of 137 sources with $S_{178} \geq S_{178}^*$, called SMS4, was created.

In 2020, a new sample of the brightest radio sources in the southern sky (White et al. 2020a,b) was generated from observations taken with the Murchison Widefield Array (MWA, Tingay et al. 2013) in the 72–231 MHz range. MWA observations obtained during the first year of operations produced the Galactic and Extragalactic All-sky MWA (GLEAM; Wayth et al. 2015) Survey, from which the Extragalactic Catalogue (EGC; Hurley-Walker et al. 2017) was built. Hence, the GLEAM 4 Jy (G4Jy) sample of 1863 sources at $\delta \leq -30^\circ$, at $|b| > 10^\circ$, and with $S_{151} > 4.0$ Jy, was established.

In recent years, significant efforts have been devoted to achieving full X-ray coverage of 3CRR sources, including a Chandra snapshot program started in 2009, beginning with sources at $z \leq 0.3$ (Massaro et al. 2010, 2012, 2015) and progressing toward higher redshifts (Massaro et al. 2013, 2018; Stuardi et al. 2018; Jimenez-Gallardo et al. 2020), coupled with follow-up observations of peculiar sources at all frequencies (see, *e.g.*, Massaro et al. 2009b; Hardcastle et al. 2010; Dasadia et al. 2016; Madrid et al. 2018; Maselli et al. 2018).

To facilitate observing all 3CRR sources with Chandra, we performed an observational campaign with Swift (Gehrels et al. 2004) for 21 3CRR sources that, according to Laing et al. (1983), were still unidentified, to increase their multifrequency information and derive accurate X-ray fluxes. With these observations, we detected X-ray emission with the Swift X-ray Telescope (XRT; Burrows et al. 2005) for 9 of the 21 objects, and we also associated an infrared counterpart with these nine and an additional four objects (Maselli

et al. 2016). The X-ray emission for seven of these nine detected sources was then investigated in greater detail with Chandra (Missaglia et al. 2021).

In this paper, we report on a Swift observing program of the SMS4 sample, including 31 sources with no X-ray observations in the Chandra or XMM-Newton archives. A total of 24 sources were observed for the first time as a result of a dedicated proposal, while six were already present in the Swift archive when our dedicated campaign started, in 2015 November. The remaining source, PKS B2148–555, was observed in 2019 February.

We performed a reduction and analysis of the Swift-XRT data and crossmatched the X-ray detections that we obtained with catalogs in the infrared and optical bands. After collecting and analyzing this multifrequency information, we compared our results with those in the literature to verify the consistency of our X-ray detections with previously suggested counterparts. The two most comprehensive and exhaustive studies that we use are White et al. (2020a,b) for infrared counterparts and Burgess & Hunstead (2006b) for optical counterparts. In the following, for the sake of simplicity, we refer to these papers as W20 and BH06, respectively.

A preliminary comparison of SMS4 with the recent G4Jy is described in Section 2; the list of observed SMS4 sources is presented in Section 3, while the reduction and analysis of Swift X-ray data are discussed in Section 4; the multifrequency analysis is described in Section 5, and our results are summarized in Section 6. Throughout this paper we use CGS units, unless otherwise stated. We also assume a flat cosmology with $H_0 = 72 \text{ km s}^{-1} \text{ Mpc}^{-1}$, $\Omega_M = 0.26$, and $\Omega_\Lambda = 0.74$ (Dunkley et al. 2009).

2. CROSSMATCH BETWEEN THE SMS4 AND G4JY SAMPLES

Despite overall similarities with the 3CRR reported by Burgess & Hunstead (2006a,b), the SMS4 is based on the extrapolation to 178 MHz of flux density values measured at 408 MHz and similarly higher frequencies, rather than on values directly measured at 178 MHz. Therefore, a fraction of sources with flux densities lower than S_{178}^* might be included in the SMS4; conversely, sources with $S_{178} > S_{178}^*$ might have been excluded.

We crossmatched the SMS4 with the G4Jy sample to establish a correspondence between sources therein, with the primary goal of determining how their actual flux density values rank with respect to the S_{178}^* threshold established in the 3CRR. Considering the extended nature of the radio emission, although with different angular sizes for each SMS4 source, we adopted a conser-

vative approach in searching for G4Jy sources within a circle centered on the SMS4 coordinates and with a radius given by the corresponding LAS, as reported in Burgess & Hunstead (2006a).

Once a match between an SMS4 source and a G4Jy source is established, we compared S_{178} from SMS4 with the total, integrated flux density, measured in the 178–185 MHz range (from here on, in this paper we indicate this quantity with \bar{S}_{181}) from G4Jy. For 78 G4Jy sources, multiple GLEAM components were associated by W20 with the same G4Jy source: in such cases, we compared S_{178} with the sum of all the \bar{S}_{181} values, each corresponding to a different GLEAM component. As a result, we find a reliable G4Jy counterpart for 127 SMS4 objects, and 47 of these have $\bar{S}_{181} < 10.9 \text{ Jy}$.

While we were able to match 127 of the 137 SMS4 sources to G4Jy sources, 10 SMS4 sources remain unmatched. Among these 10 unmatched sources, there are some of the very brightest sources at decl. $< 30^\circ$ and $|b| > 10^\circ$, which belong to a group of radio sources colloquially referred to as the *A-team*. As also reported by W20, these have been masked for the GLEAM EGC and so do not appear in the G4Jy sample. Among these 10 SMS4 sources we find Fornax A, Pictor A, Centaurus A, and a few radio galaxies in their proximity (*i.e.*, in the Centaurus Cluster), lying in the regions that were masked.

For each of these 10 sources, we searched in the literature for measurements at frequencies lower than 178 MHz in a) the observations performed with the Culgoora Circular Array (CCA) at 80 and 160 MHz (Slee 1995), in b) the survey at 145 MHz carried out with the Precision Array for Probing the Epoch of Reionization (PAPER; Jacobs et al. 2011), and in c) the 1st Alternative Data Release (ADR1) based on the survey at 150 MHz, which was carried out with the Giant Metrewave Radio Telescope (GMRT) as part of the TIFR GMRT Sky Survey (TGSS) project (Intema et al. 2017). For only one source, PKS B1318–434 (also known as NGC 5090), we did not find information in these three catalogs. For all the remaining sources, we used these data to interpolate the flux densities at 178 MHz and found that $S_{178} > 10.9 \text{ Jy}$ for all of them, as expected. As a result, excluding PKS B1318–434, we establish that $\bar{S}_{181} < 10.9 \text{ Jy}$ for 47 of 136 SMS4 sources, corresponding to a fraction of $\sim 35\%$ of the whole SMS4 sample.

3. DESCRIPTION OF OUR SAMPLE OF SMS4 SOURCES

In 2015, we compiled a list of 45 SMS4 sources, classified as radio galaxies according to BH06, that were

Table 1. List of Correspondences Established between the 31 SMS4 Sources in Our Sample and G4Jy (Top) or TGSS-ADR1 (Bottom) Sources

(1)	(2)	(3)	(4)	(5)	(6)	(7)	(8)	(9)	(10)
SMS4 Name	S_{178} (Jy)	LAS (arcsec)	Redshift	IAU Name	G4Jy ID	R.A. ($^{\circ} \ ' \ ''$)	Decl. ($^{\circ} \ ' \ ''$)	Flux Density (Jy)	Morphology
B0007–446	15.0	33	(1.00)	J001030–442259	20	00 10 30.55	–44 22 57.0	11.88±0.02	s
B0013–634	15.0	31	(> 0.56)	J001602–631005	27	00 16 02.68	–63 10 07.2	12.15±0.02	s
B0049–433	15.0	18	(0.39)	J005214–430628	93	00 52 14.88	–43 06 29.2	12.45±0.01	s
B0157–311	19.0	14	0.677	J020012–305324	213	02 00 12.15	–30 53 26.5	15.51±0.02	s
B0219–706	16.0	10	(0.40)	J022008–702231	249	02 20 08.18	–70 22 27.8	11.19±0.02	s
B0223–712	14.0	23	(1.27)	J022357–705949	257	02 23 57.55	–70 59 46.6	10.24±0.02	s
B0245–558	21.0	38	(0.82)	J024656–554116	293	02 46 56.26	–55 41 22.7	15.33±0.02	d
B0315–685	11.3	10	(1.30)	J031610–682104	339	03 16 10.10	–68 21 07.2	7.15±0.02	s
B0407–658	59.0	10	(0.77)	J040820–654458	416	04 08 20.25	–65 45 10.7	50.04±0.03	s
B0411–561	11.3	27	(0.42)	J041247–560043	427	04 12 48.02	–56 00 48.8	10.76±0.02	s
B0420–625	24.0	10	(0.81)	J042056–622337	446	04 20 56.43	–62 23 36.9	16.34±0.02	s
B0453–301	18.0	50	(0.22)	J045514–300646	506	04 55 14.31	–30 06 47.2	14.81±0.02	s
B0534–497	11.9	30	0.184	J053613–494420	563	05 36 13.67	–49 44 23.1	10.44±0.02	s
B0546–445	11.4	14	(1.15)	J054738–443114	576	05 47 38.28	–44 31 14.9	7.60±0.02	s
B0547–408	16.0	37	(0.64)	J054924–405110	580	05 49 23.49	–40 51 13.0	12.94±0.02	d
B0743–673	13.0	14	1.512	J074332–672628	672	07 43 32.63	–67 26 28.6	10.20±0.03	s
B0842–835	11.0	12	(0.82)	J083716–834440	718	08 37 14.08	–83 44 40.5	8.52±0.03	s
B0842–754	30.0	12	0.524	J084125–754033	723	08 41 26.19	–75 40 31.1	20.84±0.03	s
B0906–682	12.9	10	(> 0.56)	J090652–682940	752	09 06 52.53	–68 29 38.5	7.92±0.02	s
B1017–421	11.6	88	(0.70)	J101944–422451	836	10 19 43.84	–42 24 50.3	9.69±0.02	d
B1030–340	12.7	10	(0.50)	J103312–341842	854	10 33 13.07	–34 18 44.0	10.14±0.02	s
B1036–697	11.1	10	(0.87)	J103828–700310	862	10 38 28.27	–70 03 09.0	6.20±0.02	s
B1143–483	13.5	10	(0.33)	J114530–483606	950	11 45 30.94	–48 36 10.4	12.14±0.03	s
B1413–364	11.3	174	0.07470	J141633–364050	1135	14 16 33.65	–36 40 47.0	9.69±0.06	d
B1445–468	16.0	30	(> 0.56)	J144828–470136	1192	14 48 29.05	–47 01 39.9	10.00±0.04	s
B1451–364	20.0	123	(0.43)	J145428–364006	1203	14 54 28.53	–36 39 57.3	16.52±0.04	t
B1737–609	16.0	78	(0.41)	J174202–605519	1432	17 42 01.59	–60 55 22.4	13.74±0.04	t
B2148–555	11.6	780	0.03880	J215122–552139	1732	21 51 28.11	–55 19 45.9	6.29±0.06	t
B1247–401	12.6	10	(1.20)	J125005.7–402629	...	12 50 05.71	–40 26 29.8	13.17±1.32	...
B1346–391	13.8	19	(1.06)	J134951.0–392251	...	13 49 51.09	–39 22 51.1	12.53±1.25	...
B1358–493 ^a	13.0	51	(> 0.56)	J140131.5–493235	...	14 01 31.45	–49 32 34.8	14.31±1.02	...

NOTE—Column (1): the name in SMS4, according to the MRC or PKS (for B2148–555 only) designation. Column (2): the extrapolated flux density S_{178} . Column (3): the largest angular size of the radio source at 843 MHz. Column (4): the redshift, with lower limits and photometric estimates in parentheses. Column (5): the International Astronomical Union (IAU) name in G4Jy, according to the GLEAM designation, or in TGSS-ADR1. Column (6): the G4Jy identifier. Columns (7) and (8): R.A. and decl. of the G4Jy/TGSS-ADR1 source. Column (9): the actual flux density (\bar{S}_{181} for G4Jy, or S_{150} for TGSS-ADR1). Column (10): the radio source morphology, following W20 (s=single; d=double; t=triple).

^a - For this source two TGSS components, matching the lobes of the radio galaxy in the ATCA map published in BH06, are found. The coordinates reported in this table, matching the core, come from SUMSS.

not yet observed by Swift or Chandra or XMM-Newton. From this sample, we obtained Swift observations for 24 sources. We later included in our sample seven additional sources that, in 2021 October, among the just mentioned space missions, were observed in the X-rays only by Swift; all of these were classified as galaxies or quasars in BH06.

As described in Section 2, we were able to establish an SMS4-G4Jy correspondence for 28 out of 31 SMS4 sources. Using data from the Sydney University Mo-

longlo Sky Survey (SUMSS; Mauch et al. 2003) and the NRAO VLA Sky Survey (NVSS; Condon et al. 1998), at higher frequency than the GLEAM survey, a morphological classification was provided by W20 for all the G4Jy sources, distinguishing single (s), double (d), triple (t), and complex (c) morphology. The main difference between the double morphology and the triple morphology is the capability of detecting the core of the radio galaxy, in addition to the lobes; see W20 for further details on their morphology classification criteria. Of the 28 SMS4

sources in our sample with a G4Jy counterpart, the radio morphology is triple for three sources and is double for four sources, with all the remaining sources having a single (compact, substantially symmetric) morphology.

We notice the presence, among these 28 sources, of PKS B2148–555, which is one of the 78 G4Jy sources with which, due to their extension, more than one GLEAM component was associated by W20. High-resolution ATCA maps in Lloyd & Jones (2002) show the details of the emission of this relevant radio galaxy.

For the reasons described in Section 2, it was not possible to establish an SMS4-G4Jy correspondence for three (MRC B1247–401, MRC B1346–391, MRC B1358–493) of these 31 sources. However, for all of these, the role of G4Jy could be replaced by the TGSS, since we found matching sources in the ADR1. The correspondence that we finally establish is one-to-one for MRC B1247–401 and MRC B1346–391, while for MRC B1358–493 two nearby TGSS sources are found. Comparing the position of these two sources with the high-resolution ATCA map at 5 GHz shown in Burgess & Hunstead (2006b), one finds that they match the lobes of the radio galaxy, implying a total flux density exceeding 14 Jy. The coordinates of the single SUMSS component, lying in the middle of the two TGSS sources, match instead the core of the radio galaxy.

As a result, we finally establish a reliable correspondence for all 31 SMS4 sources, originally detected at 408 MHz, with objects in other radio catalogs at lower frequencies, in the range 150–200 MHz. All these correspondences are listed in Table 1, with those for the three SMS4 sources with no G4Jy counterpart shown at the bottom. Contrary to expectations from the original extrapolation, we find $\bar{S}_{181} < 10.9$ Jy for 14 of the 31 SMS4 objects.

We used SUMSS maps, available for all the 31 sources, to build radio flux density contours at 843 MHz. To allow the comparison between the morphology of the radio source and the underlying X-ray emission, we overlay these contours on the X-ray maps (see Figure 1) that we built from Swift-XRT observations, as described in Section 3. For G4Jy sources with double or triple morphology, we highlight the distinct SUMSS or NVSS components. For MRC B1358–493, one of the three SMS4 sources with no G4Jy counterpart, we mark the two TGSS components, matching the lobes of the radio galaxy, rather than the single SUMSS component, matching the core. For each source with multiple components, we assign a letter to each component, sorting them by decreasing flux density (A corresponding to the brighter component).

We describe here, as an example, the case of MRC B1737–609, with SUMSS contours stretched along one main direction and three resolved SUMSS components marked with A ($S_{843 \text{ MHz}} \sim 2.34$ Jy), B ($S_{843 \text{ MHz}} \sim 1.94$ Jy), and C ($S_{843 \text{ MHz}} \sim 0.64$ Jy), in agreement with the “triple” morphology classification by W20. This structure is consistent with an FR II radio galaxy, with radio jets emanating from the core (C) at some intermediate angle with respect to the observer’s line of sight and culminating in two lobes corresponding to A and B. The spatial distribution of these components is not symmetric, with A and B lying at an angular distance from C of 22'' and 55'', respectively. This asymmetry is plausibly responsible for the offset of the G4Jy centroid toward B (see Fig. 2t).

For all 31 SMS4 sources making up our sample, an optical counterpart was given in BH06 using either the plates of the UK Schmidt Southern Sky Survey or *R*-band CCD images made with the AAT. However, as we discuss in Section 5.3, we give an alternative optical source for five of these BH06 candidates. The redshift of six sources was spectroscopically measured; for the remaining 25 sources, photometric redshifts were estimated from the corresponding optical counterparts. All these redshift values are also reported in Table 1.

As a general note, considering for the G4Jy a density of one source every 13 deg² (White et al. 2020a) and the LAS values of SMS4 sources in our sample, we estimate the probability of by-chance alignment between G4Jy and SMS4 sources to be negligible. In fact, LAS values are typically lower than 50'', with few exceptions (see Table 1). Excluding the already-described case of PKS 2148–555, the highest LAS value (174'') in our sample is given by MRC B1413–364: assuming Poisson statistics, even in this less favorable case, the probability of by-chance alignment is $\sim 2 \times 10^{-4}$.

TGSS-ADR1 includes 0.62 million sources, down to ~ 11 mJy. However, for flux density values of the order of 1 Jy, the density of sources is ~ 1 source deg⁻² (see Intema et al. 2017, their Figure 9). For MRC B1358–493 (LAS = 51''), this implies a probability of by-chance alignment equal to $\sim 6 \times 10^{-4}$.

4. Swift-XRT DATA REDUCTION AND ANALYSIS

The Swift observations of the ensemble discussed here include 24 sources observed (mainly between 2015 November and 2016 September) as part of an initial Swift proposal. Among these, five sources were observed again between 2019 and 2021 by chance (MRC B1017–421 and MRC B1036–697) or from subsequent Swift Target of Opportunities (ToO) requests (MRC B0547–408,

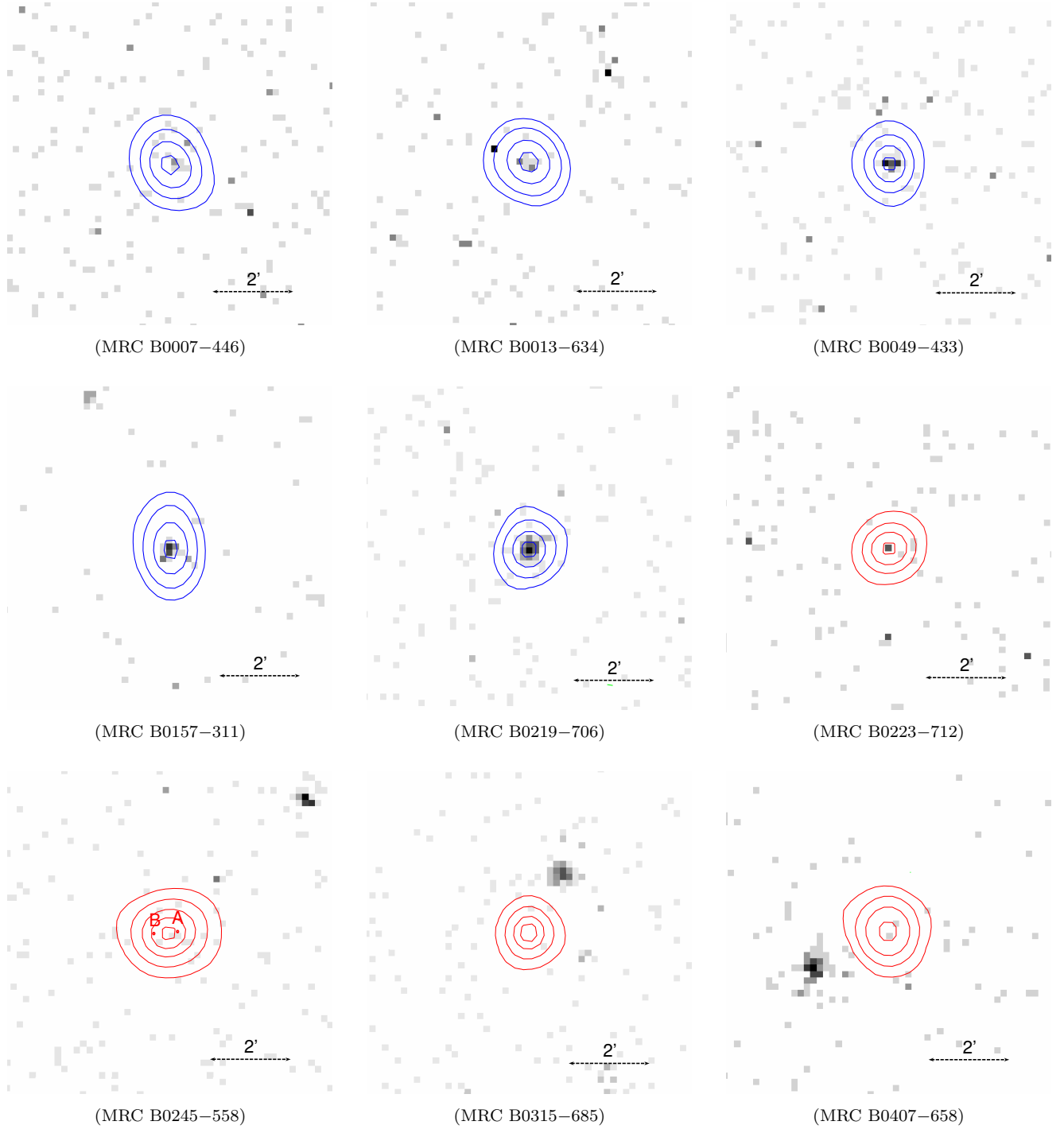


Figure 1. Swift X-ray maps in the 0.3–10.0 keV band of the 31 sources included in our sample. All maps are centered at the positions of the SMS4 radio sources. Radio flux density contours at 843 MHz from SUMSS overlay the X-ray maps, and they are shown in blue for the 20 sources detected in the X-rays by Swift and in red for the 10 sources that were not detected. Contours have been selected, for each source, to best display the shape of the radio emission. For sources with double or triple morphology, following the classification in W20, distinct SUMSS components, sorted by decreasing flux density, are shown in blue; for MRC B1358–493, distinct TGSS sources are shown in orange; for MRC B1451–364, the core, not resolved by SUMSS but by NVSS, is shown in magenta. Although PKS 2148–555 was not detected as an X-ray point source, blue contours are used also in this case, since we find significant X-ray emission at the source location on arcminute scales. As discussed in the text, PKS 2148–555 lies within the poor cluster A3816 and is associated with the cluster BCG (Lloyd & Jones 2002). The map of PKS 2148–555 ($20' \times 20'$) is binned by 16×16 pixels (1 pixel = $2''.36$). The remaining maps are binned by 4×4 pixels and are $8' \times 8'$ except for MRC B1737–609, shown at smaller scale ($4' \times 4'$).

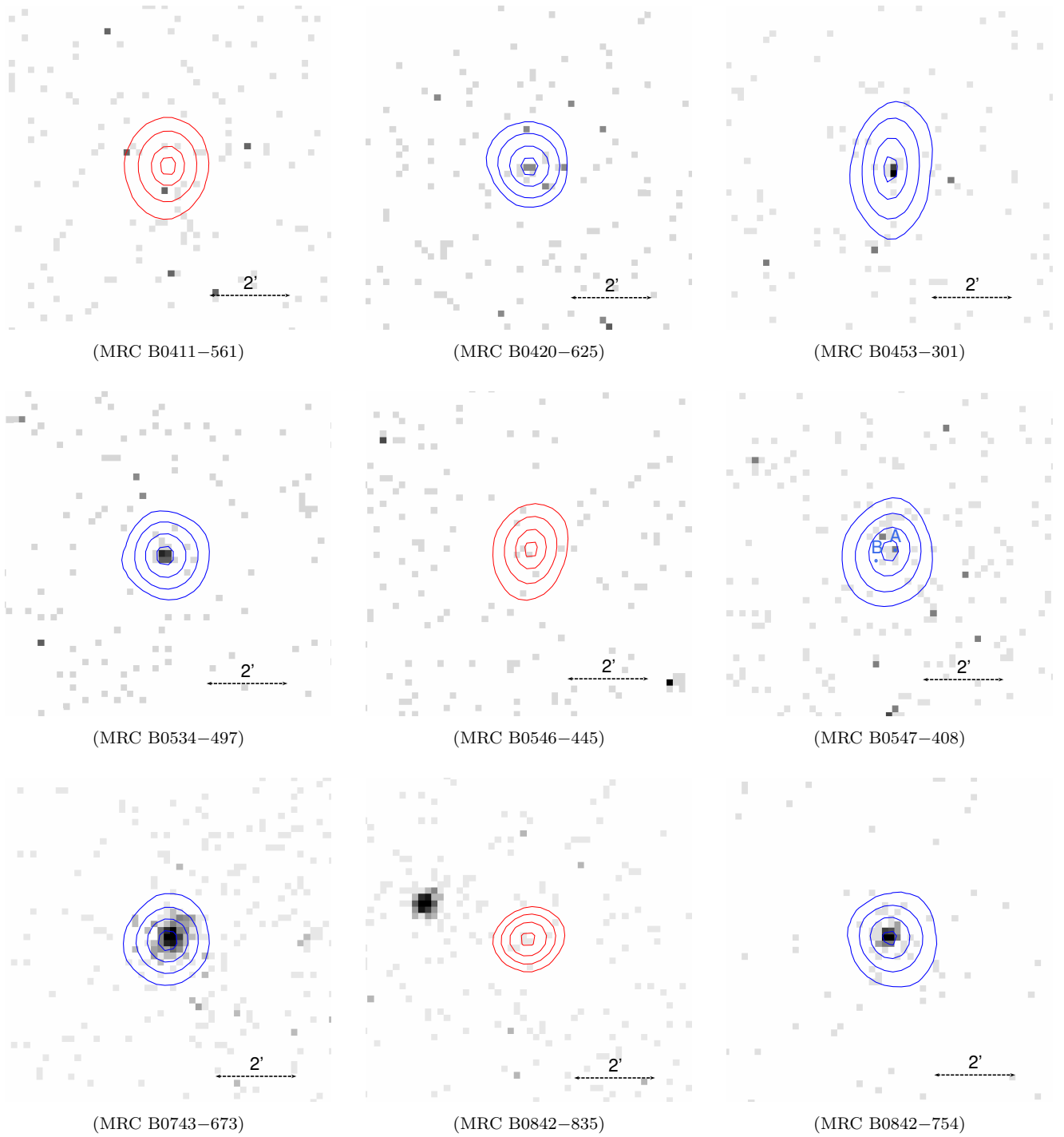


Figure 1. (*Continued.*)

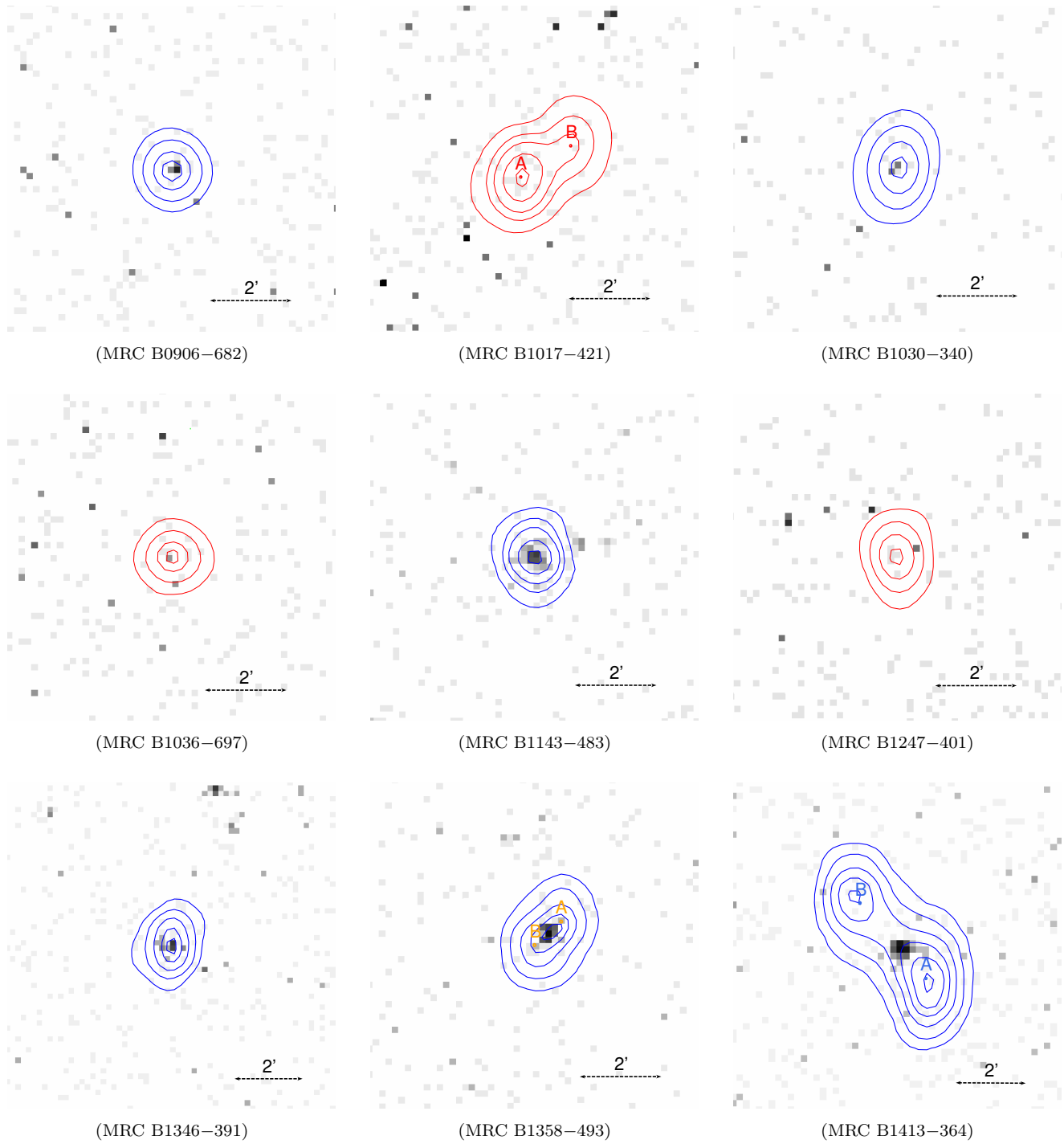


Figure 1. (*Continued.*)

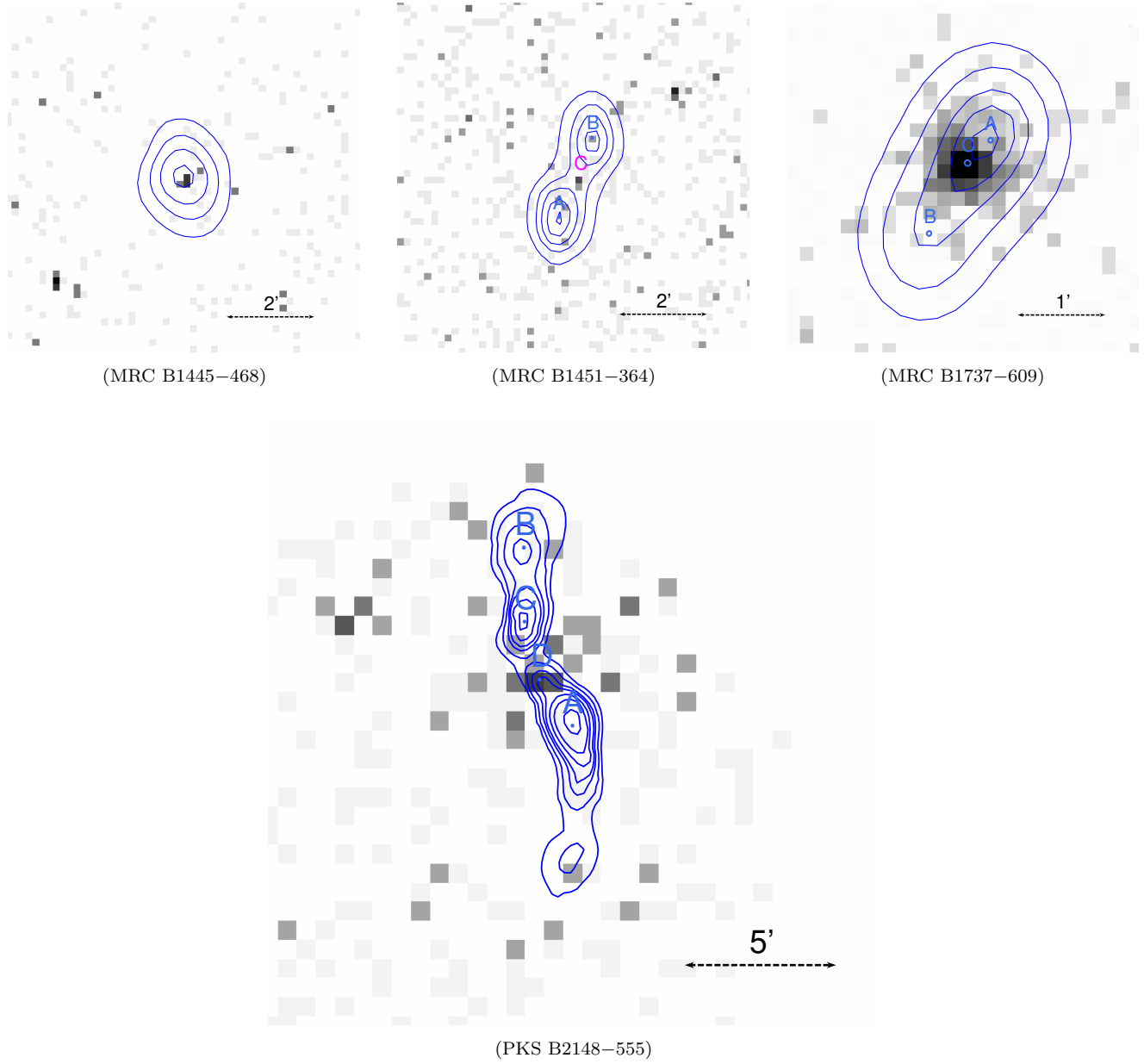


Figure 1. (Continued.)

MRC B0906–682, and MRC 1451–364). In 2021 October, the 24 sources were then supplemented with archival observations for seven additional sources: MRC B0157–311, MRC B0407–658, MRC B0743–673, MRC B0842–754, MRC B1413–364, MRC B1737–609, and PKS B2148–555. The full observational details are given in Table 2 (for detections) and Table 3 (for upper limits).

The X-ray data reduction and procedures adopted in the present analysis are analogous to those already described in Maselli et al. (2013, 2016) and references therein. Below, we briefly summarize these and include additional details, suited for the present analysis.

X-ray data from the Swift-XRT were retrieved from the Swift archive and processed with the XRTDAS software package (v3.6.0), developed at the Space Science Data Center (SSDC) of the Italian Space Agency (ASI) and distributed by the NASA High Energy Astrophysics Archive Research Center (HEASARC) within the HEASoft package (v6.28), including a collection of FTOOLS to manipulate and analyze FITS files. All the XRT observations were carried out in the most sensitive photon counting (PC) readout mode. Event files were calibrated and cleaned by applying standard filtering criteria with the XRTPipeline task and using the latest calibration files available in the Swift CALDB distributed by HEASARC. Events in the 0.3–10 keV energy range, with grades 0–12, were used in the analysis, and exposure maps were also created with XRTPipeline. For sources with several visits, event files and exposure maps from each observation were then accumulated with the XSELECT and XIMAGE tools, respectively, to build a single event file and a single exposure map for each source.

Fig. 1 shows the X-ray maps for all the 31 SMS4 sources included in our sample. To reveal X-ray emission at the position of each SMS4 source, we simultaneously uploaded both the event file and the exposure map within XIMAGE, and used the BACKGROUND command to compute the average background intensity over the whole detector. Then, we performed a local source detection using the SOSTA command within XIMAGE. This task counts the number of events within a specified box and corrects these counts for dead time, vignetting, exposure, and point-spread function (PSF). As a result, it provides the source intensity and its significance, in terms of the probability P that the signal is a statistical fluctuation of the background. If the probability is higher than $P = 10^{-3}$, a count rate 3σ upper limit is automatically calculated.

In our use of SOSTA, we fixed the side of the box to 14 pixels ($\sim 33''$), a choice that allows the core of the PSF to be fully included in the box and that, based on

our experience in the analysis of XRT images, maximizes the signal-to-noise ratio for faint sources. Furthermore, we used the qualifier `/background_level` to fix the background intensity at the value previously obtained with the BACKGROUND command. For each X-ray image, we used the cursor to precisely center the extraction box on the SMS4 coordinates. We repeated the source detection procedure adopting G4Jy coordinates in place of the SMS4 ones, which could result in the inclusion of a different number of events in the corresponding boxes, although the significance of the X-ray detections was confirmed in all cases.

Requiring $P < 10^{-4}$, which is an order-of-magnitude-tighter constraint with respect to the default in SOSTA, to establish an X-ray detection, we distinguish detections (Table 2) from nondetections (Table 3). Considering all 31 SMS4 sources, our prescriptions led to 20 X-ray detections. These correspond to two additional detections, for MRC B0547–408 and MRC B1451–364, in addition to those reported in the 2nd Swift X-ray Point Source Catalog (2SXPS; Evans et al. 2020), whose source detection relies on a blind search using a sliding cell algorithm. To determine the position, and in particular its uncertainty (90% confidence level), for all the 20 X-ray detections, we used XRTCENTROID.

4.1. The Case of PKS B2148–555

Our point-like source detection algorithm did not detect an X-ray source associated with PKS B2148–555. However, Fig. 1 definitely shows diffuse X-ray emission in the field of view (FOV) of this radio source. As reported by Lloyd & Jones (2002), this FRI radio galaxy is the brightest galaxy in Abell cluster A3816, with a largest angular size of $14'$.

The only useful observation is part of the Swift Gravitational Wave Galaxy Survey (SWGSG; see Tohuvavohu et al. 2019): its exposure is relatively short (~ 1.1 ks), with the source serendipitously in the FOV, close to the edge of the XRT detector. To reveal the thermal X-ray emission surrounding the galaxy, we filtered the event file in the 0.5–2.0 keV band and chose a circular extraction region. To reliably include this circle within a useful portion of the XRT detector, we fixed its radius at a maximum of $5'$. Using the COUNTS command within XIMAGE, we computed a total of 71 counts within this circle. After subtracting 38 counts, due to the background contribution within the same circle, we obtain a net number of 33 counts. Considering an exposure of 1034 s, corrected for the vignetting, we thus obtain a count rate of 3.2×10^{-02} counts s^{-1} . We used the NASA’s HEASARC tool WebPIMMS (v4.12a) to convert this rate into unabsorbed flux S_{unabs} : assuming the

Table 2. Swift-XRT Detections of SMS4 Sources of Our Sample

(1)	(2)	(3)	(4)	(5)	(6)	(7)	(8)	(9)	(10)
R.A. ($^{\circ} \text{ } ^m \text{ } ^s$)	Decl. ($^{\circ} \text{ } ' \text{ } ''$)	Error Radius (arcsec)	Count Rate (10^{-3} counts s^{-1})	P	First Obs. (yyyy-mm-dd)	Latest Obs. (yyyy-mm-dd)	Obs.	Exposure (s)	SMS4 Name
00 10 30.24	-44 22 55.4	6.0	1.7 ± 0.7	$3.7 \cdot 10^{-06}$	2016-01-22	2016-04-01	7	5495	B0007-446
00 16 02.80	-63 10 03.6	6.1	2.7 ± 1.1	$2.4 \cdot 10^{-07}$	2016-01-27	2016-04-24	9	3922	B0013-634
00 52 14.74	-43 06 29.8	5.3	4.9 ± 1.2	$2.2 \cdot 10^{-16}$	2015-11-30	2016-03-31	9	5667	B0049-433
02 00 12.15	-30 53 27.5	5.4	35.1 ± 6.7	$< 10^{-16}$	2015-05-03	...	1	1221	B0157-311
02 20 08.00	-70 22 29.6	4.2	26.7 ± 2.9	$< 10^{-16}$	2015-11-28	2016-04-29	10	4561	B0219-706
04 20 56.41	-62 23 41.0	5.2	2.2 ± 0.9	$3.6 \cdot 10^{-06}$	2015-12-04	2016-06-13	9	4261	B0420-625
04 55 14.05	-30 06 51.7	6.0	6.1 ± 1.7	$< 10^{-16}$	2015-12-04	2015-12-06	2	3294	B0453-301
05 36 13.83	-49 44 23.1	5.4	5.7 ± 1.4	$2.2 \cdot 10^{-16}$	2015-12-09	2016-04-17	7	4426	B0534-497
05 49 23.24	-40 51 12.1	5.6	1.5 ± 0.6	$1.2 \cdot 10^{-06}$	2015-11-28	2021-07-18	8	7052	B0547-408
07 43 32.05	-67 26 25.0	3.7	55.7 ± 3.3	$< 10^{-16}$	2009-02-16	2016-04-21	9	7266	B0743-673
08 41 27.22	-75 40 26.4	4.3	72.2 ± 8.8	$< 10^{-16}$	2011-12-24	...	1	1355	B0842-754
09 06 52.57	-68 29 37.2	5.6	1.7 ± 0.6	$1.9 \cdot 10^{-07}$	2015-12-21	2021-08-13	8	7499	B0906-682
10 33 13.45	-34 18 42.9	6.5	2.3 ± 1.0	$1.8 \cdot 10^{-06}$	2016-01-05	2016-05-27	10	4107	B1030-340
11 45 30.99	-48 36 10.2	4.1	29.0 ± 2.9	$< 10^{-16}$	2016-01-23	2016-09-22	12	4964	B1143-483
13 49 51.21	-39 22 51.2	4.7	7.2 ± 1.6	$1.1 \cdot 10^{-16}$	2015-12-17	2016-09-20	11	4306	B1346-391
14 01 31.89	-49 32 36.2	4.4	20.5 ± 2.5	$< 10^{-16}$	2015-12-16	2016-08-22	11	4746	B1358-493
14 16 33.18	-36 40 51.3	4.1	20.3 ± 2.1	$< 10^{-16}$	2013-12-20	2014-01-02	5	6807	B1413-364
14 48 28.40	-47 01 41.4	6.0	4.7 ± 1.4	$1.7 \cdot 10^{-12}$	2015-12-26	2016-05-03	8	3753	B1445-468
14 54 28.57	-36 40 04.2	4.8	1.3 ± 0.6	$3.6 \cdot 10^{-05}$	2015-12-29	2021-07-25	15	8820	B1451-364
17 42 01.41	-60 55 13.1	3.6	190.1 ± 5.5	$< 10^{-16}$	2011-11-10	2011-11-17	4	9203	B1737-609

NOTE—Columns (1) and (2): the R.A. and decl. of the X-ray detection. Column (3): the positional error radius, at the 90% confidence level. Column (4): the 0.3–10 keV count rate, with its uncertainty. Column (5): the probability P that the signal is a statistical fluctuation of the background. Columns (6) and (7): the dates of the first and the latest Swift observation. Column (8): the number of Swift observations. Column (9): the total XRT exposure time. Column (10): the name of the corresponding SMS4 source, according to the MRC designation; bold characters emphasize sources in our initial Swift proposal.

Table 3. XRT Count Rate 3σ Upper Limits at the Position of the 11 SMS4 Sources of Our sample Not Detected by Swift

(1)	(2)	(3)	(4)	(5)	(6)	(7)
SMS4 Name	First Obs. (yyyy-mm-dd)	Latest Obs. (yyyy-mm-dd)	Obs.	Exposure (s)	P	3σ Upper Limit (10^{-3} counts s^{-1})
MRC B0223-712	2015-12-03	2016-02-29	8	3822	$9.2 \cdot 10^{-02}$	3.9
MRC B0245-558	2015-12-11	2016-03-29	9	4106	$1.3 \cdot 10^{-02}$	4.3
MRC B0315-685	2015-11-29	2016-04-25	10	3731	1.0	2.4
MRC B0407-658	2013-01-03	...	1	1996	$3.5 \cdot 10^{-02}$	7.7
MRC B0411-561	2015-11-28	2016-04-21	4	4244	1.0	2.1
MRC B0546-445	2015-12-11	2016-02-05	9	3926	$1.4 \cdot 10^{-02}$	4.5
MRC B0842-835	2015-12-20	2016-01-02	6	4357	$5.4 \cdot 10^{-03}$	4.5
MRC B1017-421	2015-12-30	2019-06-25	13	5536	$5.9 \cdot 10^{-03}$	3.9
MRC B1036-697	2016-01-03	2021-04-25	10	6453	$1.3 \cdot 10^{-02}$	3.0
MRC B1247-401	2015-12-06	2016-08-23	5	4250	$9.5 \cdot 10^{-03}$	4.6
PKS B2148-555	2019-02-27	...	1	1075	$2.4 \cdot 10^{-02}$	14.9

NOTE—Column (1): the name in SMS4, with bold characters identifying sources in our initial Swift proposal. Columns (2) and (3): the dates of the first and the latest Swift observation. Column (4): the number of Swift observations. Column (5): the total XRT exposure time. Column (6): the probability P that the signal is a statistical fluctuation of the background. Column (7): the 0.3–10 keV count rate 3σ upper limit at the position of the radio coordinates.

Galactic column density, a metal abundance of 0.4 solar, and a plasma temperature $kT \sim 1.5$ keV, we obtain $S_{unabs} = 7.0 \times 10^{-13}$ erg cm $^{-2}$ s $^{-1}$. At a luminosity distance of 166.5 kpc, this implies a luminosity of 2.3×10^{42} erg s $^{-1}$, typical of a poor cluster or group (Lovisari et al. 2015). Note that varying the assumed abundance in the 0.2–1 range and the assumed temperature in the 1–5 keV range only changes the unabsorbed flux, and hence the luminosity, by $\sim 5\%$.

4.2. Extent of the X-Ray Emission

For each point source with sufficient statistics, including PKS B2148–555, which is a special case embedded in extended cluster emission, we compared the radial distribution of the detected events with the one expected from a point-like source, in order to evaluate the possible extent of the X-ray emission. The fraction of total counts within circles of varying radii, centered at the coordinates of the X-ray source, was derived by Moretti et al. (2005), who modeled the Swift-XRT PSF profile with a King function. In our analysis, we used the values computed assuming the on-axis PSF model at 1.5 keV, since most of the photons are found near this energy, where the XRT effective area peaks. We also note that the dependence of the PSF profile on energy is mild (Moretti et al. 2005).

The two regions that we used for our analysis were a circle, with a radius of 5 pixels ($\sim 12''$), and an annulus with inner and outer radii of 10 and 20 pixels, respectively. The number of counts, C and A , that we extracted from these regions, centered at the coordinates of each X-ray centroid (see Table 2), were corrected for the background contribution, computed as already reported in Section 4. The fraction $ER = C/A$ gives an estimate of the deviation of the distribution of events from a point-like source, and therefore of the extent of the X-ray emission. For each source, we then compared the ER value, reported in Table 4, with the one expected for a point-like source, which for the regions that we adopted is equal to 5.73.

The extended emission of PKS B2148–555 has already been described in Section 4.1; the results obtained following the procedure described here are also reported in Table 4 for comparison. The other two sources for which we find evidence of extended emission are MRC B0743–673 and MRC B1346–391.

The information that can be found in the literature for MRC B1346–391 is still rather poor, particularly for its emission in bands different from the radio one. Conversely, MRC B0743–673 is a well-studied source, being a flat-spectrum radio quasar (FSRQ) with a radio core-jet structure (Sadler et al. 2006), included in the

Roma-BZCAT catalog of blazars since its first edition (Massaro et al. 2009a).

The other sources listed in Table 4 do not show evidence of extended X-ray emission. For all the remaining X-ray detections, the number of counts was too low to provide statistically significant results.

4.3. Hardness Ratio and Spectral Analysis

We used the COUNTS command within XIMAGE to extract the number of counts within a circle with a radius of 10 pixels, centered at the position of our X-ray detections. We took into account the two contiguous 0.3–3 keV and 3–10 keV energy bands to distinguish soft (S) and hard (H) X-ray photons. Then, we computed the hardness ratio by means of the formula $HR = (H - S)/(H + S)$. As shown in Table 5, all sources appear to be basically soft, excluding MRC B1358–493 and MRC B1413–364. As reported below, MRC B1413–364 is also one of the two sources detected in the BAT hard X-ray catalogs.

The statistics allowed us to perform a spectral analysis with XSPEC for the seven sources with the highest count rates, among those reported in Table 5. We extracted source events from a circle with a radius of 20 pixels ($\sim 47''$), covering $\approx 90\%$ of the XRT PSF, centered at the X-ray source coordinates, and background events from a circle with a radius of 50 pixels in its proximity, avoiding eventual spurious sources. We grouped the energy spectrum files, requiring at least 20 events per bin. Then, we fitted the obtained spectra with an absorbed power law, fixing the hydrogen column density to the Galactic value (HI4PI Collaboration et al. 2016). The results of this spectral analysis are shown in Table 6: for the photon index Γ and the flux F in the 0.3–10 keV band, errors are given at a 1σ confidence level.

In most cases, statistics do not allow us to go beyond a simple power-law model fit. Using the power-law model, and leaving the n_H parameter free to vary, we find that the adoption of the n_H Galactic value adequately describes the spectrum of most sources. We report an exception to this behavior for MRC B1413–364, with an improvement of the goodness of fit given by $\chi^2 = 6.37$ (3 dof). The statistical significance of this result is given by an F -test, with a probability of 0.14 that this improvement is due to chance. The column density value that we obtain, $n_H = (2.1_{-0.9}^{+1.1}) \times 10^{22}$ cm $^{-2}$, is in excess with respect to the Galactic value (4.0×10^{20} cm $^{-2}$), suggesting the presence of intrinsic absorption. The best-fit value for the photon index is $\Gamma = 1.25_{-0.57}^{+0.63}$, significantly higher than that found fixing n_H to the Galactic value, as reported in Table 6.

Table 4. Results from the Analysis of the Extent of the X-Ray Emission

(1)	(2)	(3)	(4)	(5)
SMS4 Name	Background	C	A	ER
	(counts pixel ⁻¹)	(counts)	(counts)	
MRC B1737–609	$1.08 \cdot 10^{-2}$	1055	193	5.47 ± 0.56
MRC B0743–673	$3.71 \cdot 10^{-3}$	230	68	3.40 ± 0.64
MRC B1413–364	$1.08 \cdot 10^{-3}$	80	16	5.09 ± 1.85
MRC B1143–483	$4.11 \cdot 10^{-3}$	78	16	4.82 ± 1.75
MRC B0219–706	$3.11 \cdot 10^{-3}$	72	11	6.48 ± 2.71
MRC B0842–754	$1.17 \cdot 10^{-3}$	57	14	4.10 ± 1.64
MRC B1358–493	$2.91 \cdot 10^{-3}$	48	9	5.16 ± 2.44
MRC B0157–311	$1.19 \cdot 10^{-3}$	24	3	8.30 ± 6.59
MRC B1346–391	$4.48 \cdot 10^{-3}$	16	7	2.31 ± 1.47
PKS B2148–555	$1.30 \cdot 10^{-2}$	1	5	0.19 ± 0.28

NOTE—Column (1): the name of the SMS4 source. Column (2): the measured number of background counts, per pixel. Column (3): the background-corrected number of counts C within a circle with a radius of 5 pixels. Column (4): the background-corrected number of counts A within an annulus with inner and outer radii of 10 and 20 pixels, respectively. Column (5): the extent ratio ER , with its 1σ error.

Table 5. Results from the Analysis of the Hardness Ratio of X-Ray Detections

(1)	(2)	(3)	(4)
SMS4 Name	S	H	HR
	(counts)	(counts)	
MRC B1737–609	1199	222	-0.69 ± 0.02
MRC B0743–673	258	49	-0.68 ± 0.04
MRC B1413–364	42	67	0.23 ± 0.16
MRC B1143–483	94	15	-0.72 ± 0.05
MRC B0219–706	78	14	-0.70 ± 0.06
MRC B0842–754	56	17	-0.53 ± 0.10
MRC B1358–493	30	41	0.15 ± 0.19
MRC B0157–311	24	5	-0.66 ± 0.12
MRC B1346–391	27	4	-0.74 ± 0.10

NOTE—Column (1): the name of the SMS4 source. Column (2): the measured number of counts S in the soft (0.3–3 keV) band. Column (3): the measured number of counts H in the hard (3–10 keV) band. Column (4): the hardness ratio HR , with its 1σ error.

Table 6. Results from the Spectral Analysis

(1)	(2)	(3)	(4)	(5)	(6)
SMS4 Name	Counts	$n_{H, Gal}$	Γ	$F_{0.3-10 keV}$	χ^2/dof
		(cm ⁻²)		(10^{-12} erg cm ⁻² s ⁻¹)	
B1737–609	1606	$6.2 \cdot 10^{20}$	$1.80^{+0.04}_{-0.04}$	$7.6^{+0.3}_{-0.3}$	64.63/69
B0743–673	366	$8.9 \cdot 10^{20}$	$1.60^{+0.08}_{-0.08}$	$2.6^{+0.3}_{-0.2}$	20.87/16
B1413–364	121	$4.0 \cdot 10^{20}$	$-0.24^{+0.16}_{-0.18}$	$3.1^{+0.4}_{-0.6}$	15.09/4
B1143–483	120	$1.0 \cdot 10^{21}$	$1.75^{+0.17}_{-0.17}$	$1.0^{+0.1}_{-0.2}$	2.85/4
B0219–706	103	$6.1 \cdot 10^{20}$	$1.55^{+0.15}_{-0.15}$	$1.1^{+0.1}_{-0.1}$	3.20/3
B0842–754	81	$7.4 \cdot 10^{20}$	$1.40^{+0.18}_{-0.19}$	$3.5^{+0.8}_{-0.6}$	7.30/2
B1358–493	80	$1.5 \cdot 10^{21}$	$-0.20^{+0.23}_{-0.24}$	$3.4^{+0.5}_{-0.7}$	1.93/2

NOTE—The analysis was carried out using an absorbed power law, fixing the hydrogen column density to the Galactic value. Column (1): the MRC name of the SMS4 source. Column (2): the number of counts in the spectrum, corrected for the background contribution. Column (3): the Galactic hydrogen column density $n_{H, Gal}$. Column (4): the corresponding photon index Γ , with its 1σ error. Column (5): the absorbed flux in the 0.3–10 keV band, with its 1σ error. Column (6): the χ^2 value, with the number of degrees of freedom.

Only 2 of the 20 sources detected with the XRT, MRC B1413–364 and MRC B1737–609, are detected in the two series of the catalogs (Tueller et al. 2010; Segreto et al. 2010) produced with data from the Swift Burst Alert Telescope (BAT; Barthelmy et al. 2005). In the hard BAT telescope band (14–195 keV), SWIFT J1416.5–3671 is brighter than SWIFT J1742.1–6054¹, consistent with our HR analysis, reported in the discussion above and in Table 5.

5. MULTIFREQUENCY ANALYSIS

In this section, we first discuss the matching of the SMS4 radio sources with the detected Swift sources and establish the radio/X-ray association when the radio and the X-ray positional uncertainties overlap. We show that the probability of chance coincidence between a Swift detection and an SMS4 source is negligible. We then discuss the WISE and optical identifications, mainly utilizing the X-ray position. The association with infrared or optical sources is allowed only if their coordinates lie within the corresponding X-ray positional uncertainty.

All the sources in our sample were classified by BH06 as quasars and radio galaxies. In the optical band, emission from the AGN itself, but likely also from the host galaxy, can be detected. In type II AGNs, the nuclear optical emission might be absorbed and obscured, but the infrared is more likely to reach the observer. In our efforts to localize the core of the AGN, with our multi-frequency analysis, we adopt a simple but conservative criterion, requiring a detection in both the infrared and optical bands.

As a preliminary step to match our X-ray detections with infrared and optical counterparts, we used the SkyView Virtual Observatory to retrieve infrared maps in the W1 filter (3.4 μm) from the AllWISE Data Release (Cutri et al. 2014) Images Atlas and optical maps in the r filter (0.62 μm) from the Space Telescope Science Institute (STScI) 2nd Digitized Sky Survey (DSS2). With these maps, we built the panels shown in Fig. 2.

Next, we used TOPCAT to crossmatch our list of X-ray detections with sources from selected radio, infrared, and optical catalogs.

5.1. Identifying X-Ray Sources with Radio Sources

To reliably associate our 20 X-ray-detected sources, listed in Table 2, with corresponding radio sources, we

matched the source positions at these two energy ranges. We used G4Jy (W20) as the main matching radio catalog for the 18 sources that were surveyed by GLEAM, and SUMSS for the remaining two sources (see Table 1). Following W20, the typical rms positional uncertainties for G4Jy sources are $\sigma_{\alpha,S} \approx 1''.5$, $\sigma_{\delta,S} \approx 1''.7$, when their brightness-weighted centroids were computed after a cross-correlation with SUMSS data, while they are $\sigma_{\alpha,N} \approx 0''.5$, $\sigma_{\delta,N} \approx 0''.6$, when the same operation was based on NVSS data.

To match the radio and X-ray positions, we conservatively use a circular confidence region that is sufficiently large to ensure, with high probability, that the radio source lies within the X-ray positional error region. For this circular region, we use a radius r_X corresponding to the error radius, at 90% confidence level, for sources at the X-ray limit of sensitivity, to which we add the largest uncertainty r_r for the radio position, at the same confidence level as for the X-rays. For the X-ray band, we find $r_X = 6''.5$ from Table 2. For the radio band, we take the larger between $\sigma_{\alpha,S}$ and $\sigma_{\delta,S}$, and multiply it by a factor of 1.645, derived from the Normal distribution, obtaining $r_r = 2''.8$. Using a circle with $R = r_r + r_X = 9''.3$, we find that the combined 90% confidence positional uncertainty totally includes the corresponding G4Jy or SUMSS positional uncertainty for all Swift-XRT detections. For MRC B1737–609, we assume the SUMSS C component matches the core, as discussed in Section 3, rather than the G4Jy position; in any case, also taking into account the G4Jy centroid itself, the X-ray positional uncertainty covers half of that in the radio band.

After obtaining matches for all our X-ray-detected sources with corresponding radio sources, we computed the probability that these matches might be due to chance. As a first step, we used WebPIMMS to estimate the flux in the 0.5–2.0 keV band for sources at the limit of sensitivity. We converted the lowest count rate (1.3×10^{-3} counts s^{-1}) obtained from our XRT detections, using a power-law model and adopting reasonable spectral assumptions ($n_H = 4 \times 10^{20}$ cm^{-2} , $\Gamma = 1.7$), to obtain $F_{0.5-2 \text{ keV}} \simeq 2 \times 10^{-14}$ $\text{erg cm}^{-2} \text{ s}^{-1}$. Using the log N -log S distribution published by Gilli (2004), we derive a density of ~ 30 sources deg^{-2} brighter than our flux limit. Considering that the XRT FOV corresponds to $\sim 5.6 \times 10^2$ arcmin^2 , ≈ 5 random X-ray sources are expected in each XRT FOV.

In the conservative case of a combined, 90% confidence positional uncertainty given by a circle with a radius $R = 9''.3$, five serendipitous X-ray sources cover an area $S_5 \sim 0.38$ arcmin^2 . This implies that the chance of a radio/X-ray overlap, in any one field, is at most

¹ Using the data from the 157-Month catalog (<https://swift.gsfc.nasa.gov/results/bs157mon/>), SWIFT J1416.5–3671 has a flux of $(14.71_{-3.18}^{+3.87}) \cdot 10^{-12}$ $\text{erg cm}^{-2} \text{ s}^{-1}$, while SWIFT J1742.1–6054 has a flux of $(5.71_{-2.10}^{+2.26}) \cdot 10^{-12}$ $\text{erg cm}^{-2} \text{ s}^{-1}$.

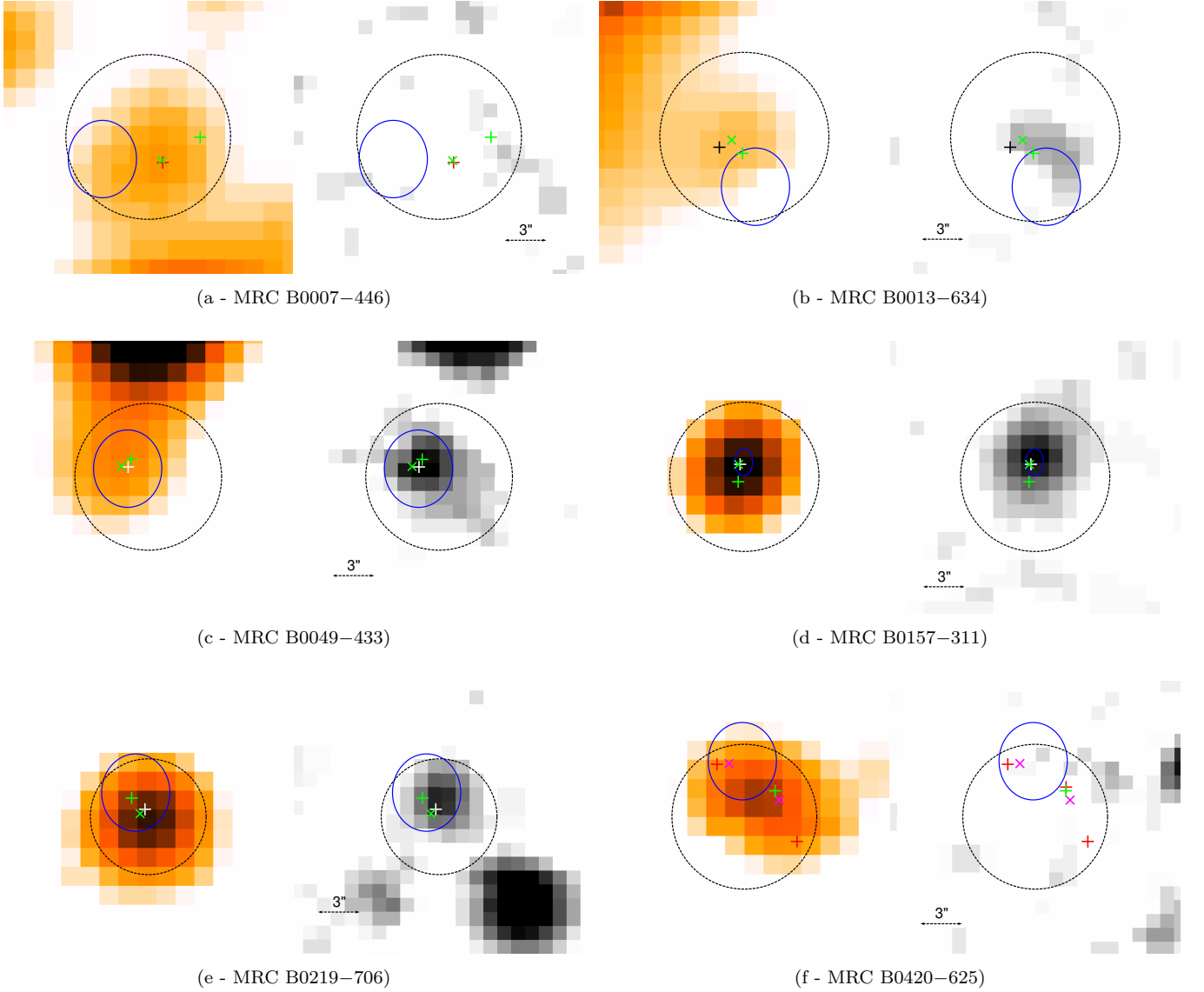


Figure 2. Infrared and optical maps, at the same scale, of the 20 SMS4 sources detected by Swift-XRT in our sample. Infrared maps (left side of each panel) in the W1 filter ($3.4 \mu\text{m}$) are from AllWISE, while optical maps (right side; 1 pixel= $1''$) in the r filter are from DSS2. Ellipses mark the positional uncertainty of radio sources: blue is used for G4Jy; magenta is used for SUMSS in panels (o), (p), and (t); and red is used for NVSS in panel (s). Black dashed circles mark the positional uncertainty of the X-ray sources. Positional uncertainties are given at 90% confidence level for both the radio and the X-ray sources. Crosses (x) and plus signs (+) mark infrared and optical sources, respectively. Green is used for counterparts associated by W20 and by BH06. For other AllWISE and GSC 2.3.2 sources, black or white are equally used to improve the visibility with respect to the map in the background. In the infrared band: in panels (f), (l), (m), and (r), magenta crosses mark sources from CatWISE2020. In the optical band: in panels (a), (f), (h), and (i), red plus signs mark sources from DES DR2.

$P \sim S_5/\text{FOV} \sim 6.7 \times 10^{-4}$. In our complete sample of 31 fields, the expected number of spurious matches is $31 \times P = 0.021$. Hence, the probability of spurious coincidences between X-ray and radio sources is very small.

5.2. Crossmatches with Infrared and Optical Catalogs

In the infrared band, the main catalog that we adopted in our crossmatch with the Swift sources is AllWISE. The typical positional uncertainties are

in the range $0''.03$ – $0''.08$, with only one source (J001030.14–442257.1) with an uncertainty of $0''.3$. In addition, we searched for counterparts in the CatWISE2020 (Marocco et al. 2021) catalog, which benefits from much longer exposure times and improved source detection algorithms with respect to AllWISE.

In the optical band, the main catalog that we used for source identification is the Second Generation Guide

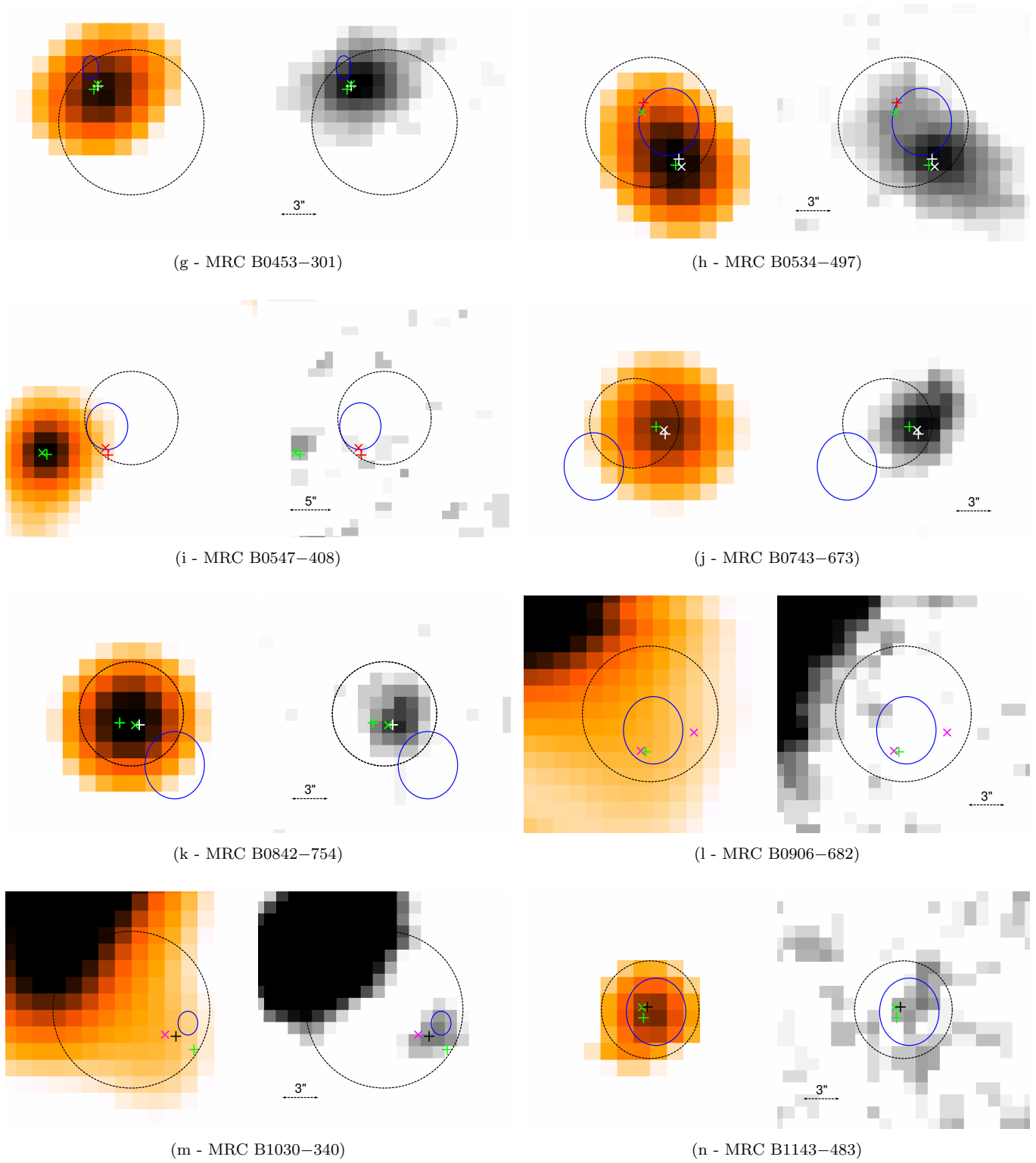


Figure 2. *(Continued.)*

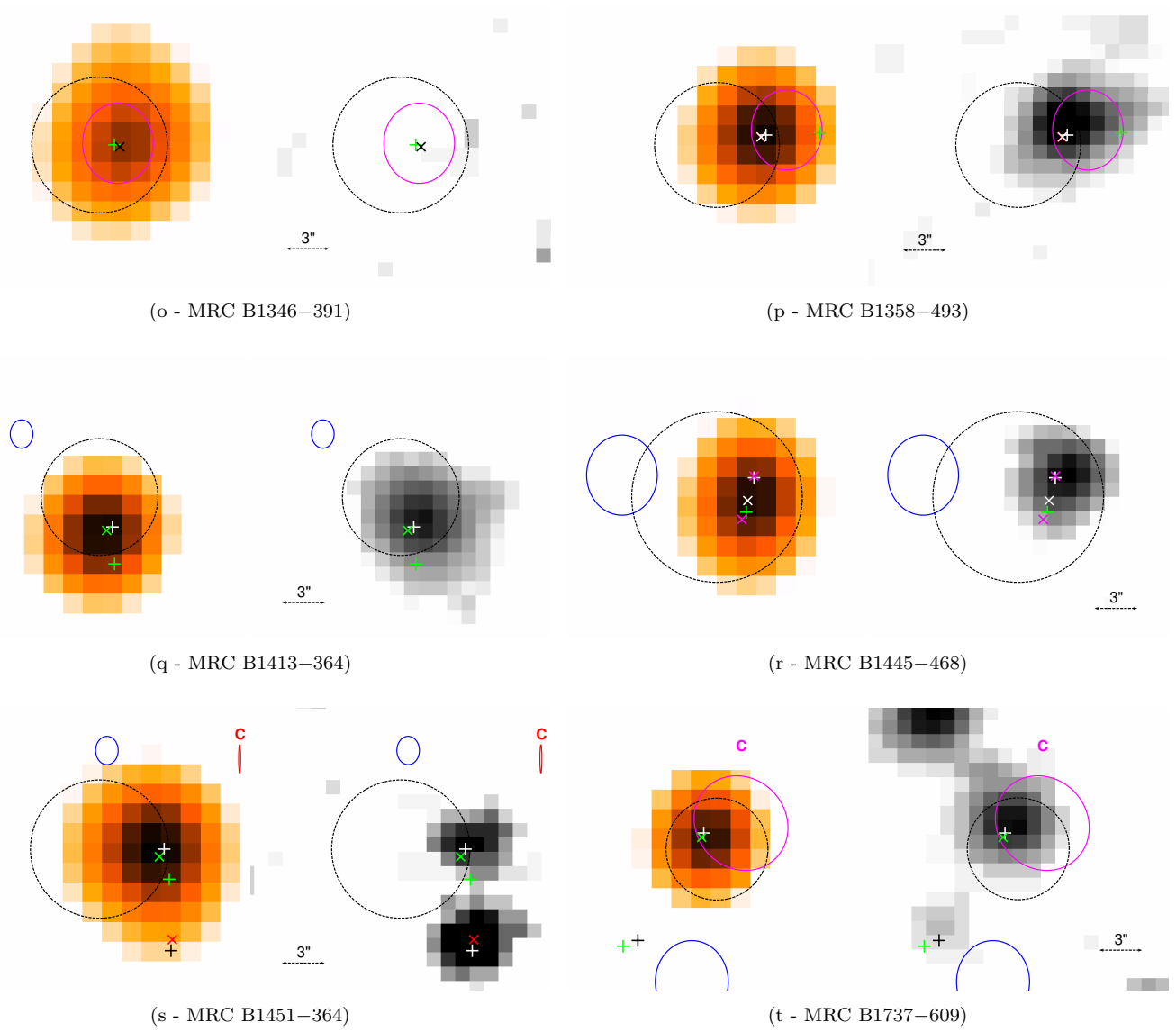


Figure 2. *(Continued.)*

Star Catalog (GSC 2.3.2) by Lasker et al. (2008), which has a typical positional uncertainty in the $0''.26$ – $0''.40$ range. In addition, we searched the Dark Energy Survey (DES) Data Release 2 (DR2; Abbott et al. 2021).

In our analysis, we took into account the infrared color of our WISE candidates, comparing $W1$ – $W2$ with the threshold ($W1$ – $W2 \geq 0.8$ mag) established by Stern et al. (2012) in their simple criterion for selecting AGNs. Furthermore, we searched for our candidates in previously selected AGN (Edelson & Malkan 2012; Secrest et al. 2015) and quasar (Soucay et al. 2019) samples, to strengthen the hypothesis of their extragalactic nature.

As a result of our analysis, we find at least one candidate counterpart, detected in both the infrared and the optical bands, for all our SMS4 sources. However, we distinguish two classes according to the reliability of the optical and WISE counterparts. Class A sources are those whose candidate counterpart is unique since it lies within the XRT positional uncertainty at the 90% confidence level and shows typical AGN colors. Class B sources are those having more than one plausible candidate within, or in the proximity of, the XRT positional uncertainty (90% c.l.). All our candidate counterparts are listed in Table 7.

To estimate the probability that our counterparts, all with a detection in both the infrared and the optical bands, are by chance aligned with the corresponding X-ray source, we can consider the AllWISE infrared sources alone. The $W1$ magnitudes of our sources lie in the 11.5–17.1 mag range (see Table 7), with a mean magnitude of $W1 = 14.1$ mag. From the Explanatory Supplement to the AllWISE Data Release Products (Cutri et al. 2013; see Figure 6a at https://wise2.ipac.caltech.edu/docs/release/allwise/expsup/sec2_1.html), we derived the density of sources with $W1 \leq 14$ mag, which is $\sim 1.1 \times 10^3$ sources deg^{-2} . In a circle with a radius equal to R (see Section 5.1), $\sim 2.29 \times 10^{-2}$ sources are then expected. For the faintest infrared counterpart (MRC B0007–446) with magnitude $W1 = 17.1$ mag, the IR source density to this faint limit implies 0.24 sources per $R = 9''.3$ radius circle.

5.3. Comparison with Earlier Studies

While all infrared counterparts associated by W20 are AllWISE sources, optical counterparts were associated by BH06 using either the plates from the UK Schmidt Southern Sky Survey or R -band CCD images from a dedicated campaign at the AAT. We notice that, despite an overall agreement between the coordinates reported in the GSC 2.3.2 catalog and those reported by BH06, they do not strictly coin-

cide. In four cases (MRC B1358–493, MRC B1413–364, MRC B1445–468, and MRC B1451–364) the angular separations between GSC 2.3.2 and the optical coordinates given by BH06 exceed $2''$, and thus do not allow us to conclude that they are the same astrophysical objects. Thus, when both the GSC 2.3.2 and the BH06 sources are available and they most likely refer to the same object, we validate the BH06 counterpart, even though we report the GSC 2.3.2 source in Table 7. As discussed below in this section, we treat MRC B1445–468 in the same way; for the remaining three aforementioned sources, we validate the GSC 2.3.2 source as the optical counterpart, rather than the BH06 association.

W20 associated an infrared counterpart to 13 of the 20 SMS4 sources for which Swift detected X-ray emission, while optical counterparts were associated by BH06 with each of them. The W20 counterparts are reliably matched by the BH06 counterpart for 8 of the 13 SMS4 sources: MRC B0013–634, MRC B0049–433, MRC B0157–311, MRC B0219–706, MRC B0453–301, MRC B0547–408, MRC B0842–754, and MRC B1143–483. In the remaining five cases, the match is questionable (MRC B0007–446, MRC B1413–364, and MRC B1451–364) or does not occur (MRC B0534–497 and MRC B1737–609) owing to the large angular separation.

The counterparts of seven among the eight reliable matches described above lie within the corresponding XRT positional uncertainty regions (90% c.l.). Conversely, for MRC B0547–408, W20 and BH06 counterparts lie $5''.7$ from the boundary of this X-ray region. Typical AGN-like WISE colors characterize this infrared source. Within the same X-ray region, a faint infrared source from CatWISE2020 matches an optical source from DES DR2. We note that the X-ray positional uncertainty, computed using eight counts, fully includes the radio G4Jy centroid, with its positional uncertainty (90% c.l.). However, due to the double radio morphology of MRC B0547–408 (see Section 3 and Figure 1), the position of this G4Jy centroid, lying between the SUMSS lobe components, might not match the actual core position. For these reasons, the bright WISE candidate, previously selected by W20, and its corresponding optical counterpart selected by BH06, might be the correct match to the radio and X-ray source, even though it lies $11''.3$ from the X-ray position.

Focusing on class A sources, there are 12 sources for which the optical and WISE/IR positions are in excellent agreement. There are an additional six sources where the optical/WISE coordinates differ by more than $2''$ from the optical candidates given in BH06. For four WISE sources from W20, we find an alter-

Table 7. Our Candidate Counterparts for X-Ray-Detected SMS4 Sources

(1) SMS4 Name	(2) Class	(3) Infrared Source	(4) W1 (mag)	(5) W1–W2 (mag)	(6) Optical Source	(7) Δ (arcsec)
B0007–446	A	AW J001030.14–442257.1 ^a	17.09	0.59	DES J001030.13–442257.4	0.34
B0013–634	A	AW J001602.93–631003.8 ^a	14.65	0.49	GSC2.3 S19X010969	1.03
B0049–433	A	AW J005214.91–430629.0 ^a	14.29	1.02	GSC2.3 S2SX008795	0.50
B0157–311	A	AW J020012.17–305326.6 ^a	13.35	1.06	GSC2.3 S2YS004732	0.11
B0219–706	A	AW J022008.11–702229.3 ^a	14.14	1.24	GSC2.3 S1G6004776	0.48
B0420–625 ^g	B	CW J042056.03–622339.8	16.19	0.34	BH06 J042056.09–622339.1	0.76
B0453–301	A	AW J045514.26–300648.5 ^a	13.94	0.47	GSC2.3 S239004216	0.14
B0534–497 ^g	B	AW J053613.56–494426.8	14.21	0.28	BH06 J053613.61–494426.7	0.49
B0547–408 ^b	A	AW J054924.17–405116.2 ^a	15.06	1.52	GSC2.3 S1ZG001633	0.58
B0743–673	A	AW J074331.61–672625.5	13.16	0.93	GSC2.3 S4MI002100	0.37
B0842–754	A	AW J084127.07–754027.7 ^a	13.12	0.94	GSC2.3 S43L002329	0.36
B0906–682	A	CW J090652.71–682940.2	15.84	0.34	BH06 J090652.64–682940.3	0.41
B1030–340	A	CW J103313.22–341844.9	15.34	0.65	GSC2.3 S5M4020229	0.89
B1143–483	A	AW J114531.05–483610.0 ^a	13.67	1.11	GSC2.3 S45R029125	0.42
B1346–391	A	AW J134951.08–392251.3	14.90	0.60	BH06 134951.12–392251.2	0.40
B1358–493	A	AW J140131.57–493235.5	11.74	1.16	GSC2.3 S96M055339	0.36
B1413–364 ^c	A	AW J141633.15–364053.7 ^a	12.29	1.03	GSC2.3 S9AR000360	0.48
B1445–468 ^d	A	AW J144828.18–470141.6	13.78	0.68	GSC2.3 S9DJ002907	1.55
B1451–364 ^e	A	AW J145428.22–364004.7 ^a	14.52	0.25	GSC2.3 S9H2063281	0.63
B1737–609 ^f	A	AW J174201.49–605512.2 ^a	11.55	0.94	GSC2.3 S7FE029330	0.34

NOTE—Column (1): the SMS4 name, according to the MRC designation. Column (2): the class, reflecting the reliability of the candidate’s association (see Section 5.2). Column (3): the infrared source identification (AW: AllWISE, [Cutri et al. 2014](#); CW: CatWISE2020, [Marocco et al. 2021](#)). Column (4): the WISE magnitude in the W1 filter. Column (5): the WISE W1–W2 infrared color. Column (6): the optical source identification. Column (7): the angular separation Δ between the given infrared and optical sources.

^a This infrared source was previously associated by W20.

^b Bright infrared source, at the boundaries of the XRT 99% positional uncertainty, with WISE AGN-like colors.

^c Extended radio galaxy (see Figure 1), with low-frequency G4Jy centroid not reliably matching the core; the BH06 optical counterpart lies 2’’6 from the GSC 2.3.2 source.

^d The BH06 counterpart lies $\sim 2''5$ from the GSC 2.3.2 source; the AllWISE source lies between these optical sources.

^e Extended radio galaxy (see Figure 1), with low-frequency G4Jy centroid not reliably matching the core; the XRT positional uncertainty (90% c.l.) includes only one of two close sources.

^f Candidate matching the SUMSS C component of an extended radio galaxy, consistent with its radio core.

^g As discussed in the text, there are two viable counterparts. The given source IDs are those that include, as an optical counterpart, the one suggested in BH06 (the green plus sign in Fig. 2).

native optical candidate to that in BH06, either in GSC 2.3.2 (MRC B1413–364, MRC B1451–364, and MRC B1737–609) or in DES DR2 (MRC B0007–446). Although MRC B1358–493 and MRC B1445–468 have no WISE match listed in W20, we do find WISE counterparts for both sources and matching optical counterparts. We discuss each of these six sources:

- MRC B0007–446: as shown in Fig. 2a, we find an optical source, detected in DES DR2 rather than in GSC 2.3.2, matching the W20 counterpart; no infrared counterpart is found for the BH06 candidate.
- MRC B1358–493: missing in GLEAM EGC (see Section 2), W20 could not provide an infrared counterpart for this SMS4 source. However, an AllWISE source with an infrared color (W1–W2 = 1.16 mag) fully consistent with AGNs, matched by a GSC 2.3.2 source, lies within the XRT positional uncertainty (90% c.l.). The coordinates given by BH06 are slightly different. The AllWISE source was already included in the W2 sample of [Edelson & Malkan \(2012\)](#).
- MRC B1413–364: the coordinates of both the W20 infrared and the BH06 optical candidates (Fig. 2q) match a source that appears extended in the maps. According to [Simpson et al. \(1993\)](#), it is a galaxy at $z = 0.075$. We find a GSC 2.3.2 source matching the W20 counterpart (W1–W2 = 1.03 mag), that was already included both in the W2 sample of [Edelson & Malkan \(2012\)](#) and in the AGN catalog of [Secrest et al. \(2015\)](#). For this reason, we give this GSC source as the optical

counterpart, rather than the BH06 choice that lies outside the XRT positional uncertainty.

- MRC B1445–468: the angular separation between the BH06 counterpart and the GSC 2.3.2 source is $\sim 2''.5$: this, in principle, would not guarantee that these objects match each other. However, a single infrared source, detected in AllWISE, lies between the aforementioned optical sources, at $0''.9$ and $1''.6$ from the BH06 and the GSC 2.3.2 source, respectively. Thus, assuming a reliable association with the AllWISE source, whose infrared color ($W1 - W2 = 0.68$ mag) is close to the 0.8 mag threshold, we have no strong evidence to discard the BH06 counterpart: similar to other cases, we validate this counterpart, reporting at the same time the GSC 2.3.2 source in Table 7.
- MRC B1451–364: the difficulty of determining the optical counterpart was first raised by the analysis carried out by Jones & McAdam (1992), who quoted four different candidates. BH06 also noted more than one candidate. The conclusions of both these studies were not in agreement, with BH06 supporting a “diffuse object” among the four previously reported by Jones & McAdam (1992). The position of this BH06 candidate, marked by a green plus sign in Fig. 2s, lies in the middle of two GSC 2.3.2 sources. The XRT positional uncertainty (90% c.l.) includes only one of these, also matching the W20 infrared counterpart, AllWISE J145428.22–364004.7, with $W1 - W2 = 0.25$ mag. The other GSC 2.3.2 source also matches an infrared source (CatWISE2020 J145428.15–364010.4), with infrared color $W1 - W2 = -0.02$ mag, even lower than the AllWISE source.
- MRC B1737–609: the angular separation between counterparts given by W20 and BH06 (Fig. 2t) is $\sim 9''.5$. The Swift-XRT circular region of uncertainty at 90% confidence level includes the infrared source selected by W20 ($W1 - W2 = 0.91$ mag), also detected in the optical, at variance with the BH06 candidate. Also in this case, the extragalactic nature of this infrared source is supported by its inclusion in both the Edelson & Malkan (2012) and the Secrest et al. (2015) AGN samples. The same X-ray circle also matches the SUMSS component, named C in both Figure 1 and Fig. 2t, corresponding to the core of the radio galaxy (see Section 3). An optical spectrum, obtained by Rojas et al. (2017) for the object corresponding to our AllWISE/GSC 2.3.2 counterpart, revealed broad

emission lines over a continuum emission, leading to a redshift $z = 0.152$.

In addition to the eight sources with reliable BH06-W20 counterpart matches, the seven remaining SMS4 sources for which we validate the BH06 counterparts are five class A sources (MRC B0743–673, MRC B0906–682, MRC B1030–340, MRC B1346–391, and MRC B1445–468) and the two class B sources (MRC B0420–625 and MRC B0534–497). To these five class A sources, and also to the already-mentioned MRC B1358–493, we provide an infrared counterpart for the first time, since they were not associated by W20.

Finally, we describe in greater detail the two remaining class B sources, for which we could not establish firm conclusions about the counterpart.

- MRC B0420–625: as shown in Fig. 2f, neither an infrared source in the AllWISE Data Release nor an optical source in the GSC 2.3.2 was detected for MRC B0420–625 within the XRT error circle. However, two infrared sources were detected in CatWISE2020, and both are coincident with optical sources detected in DES DR2. One of these infrared sources, CatWISE2020 J042056.03–622339.8 ($W1 - W2 = 0.34$ mag), is closer to the center of the source that appears extended in the infrared map, and it matches the optical counterpart found by BH06. The other source, CatWISE2020 J042056.55–622337.1 ($W1 - W2 = 0.29$ mag), lies at the outskirts of the extended source. Additional information is needed to determine the counterpart.
- MRC B0534–497: both maps in Fig. 2h show an extended source, with two AllWISE sources separated by $5''.5$, on opposite sides of the radio ellipse of G4Jy#563. One of the AllWISE sources, AllWISE J053613.90–494422.2 ($W1 - W2 = 0.71$ mag): marked by a green cross, corresponds to the counterpart given by W20, and is matched by a DES DR2 source ($r=21.1$ mag). The other source is AllWISE J053613.56–494426.8 ($W1 - W2 = 0.28$ mag): shown in white, it lies at the center of the extended source in the maps and matches a much brighter optical source ($R=16.5$ mag), detected in GSC 2.3.2; it corresponds to the optical counterpart suggested by BH06.

6. SUMMARY AND CONCLUSIONS

In 2006, the SMS4 was compiled by extrapolating the flux density, measured at higher frequencies, to

178 MHz, rather than by using actual measurements at that frequency. Since 2020 the G4Jy (White et al. 2020a) has been available, and we crossmatched the SMS4 sample with the G4Jy sample to establish correspondences between sources. For the 10 SMS4 sources lacking matches in the G4Jy, data collected from other low radio frequency catalogs were retrieved. Based on these data, we establish a fraction of $\sim 35\%$ of SMS4 sources with flux density at 178 MHz (or comparable frequency) lower than 10.9 Jy, at variance with the extrapolated values. This result confirms and quantifies the intrinsic selection effect in the SMS4 sample and definitely encourages the use of G4Jy for future comparison with the 3CRR in the Northern Hemisphere.

In 2015, we obtained observations with Swift for 24 sources classified as radio galaxies by Burgess & Hunstead (2006b), but not yet observed by either Chandra, Swift, or XMM-Newton. We complemented this list with the seven SMS4 sources observed only by Swift, among the just mentioned missions, and report here detections with the Swift-XRT for 20 of the 31 sources in our sample; 6 of these 20 correspond to less luminous radio sources, with $\bar{S}_{181} \leq 10.9$ Jy. Furthermore, we highlight the presence of diffuse X-ray emission in the FOV of PKS B2148–555, which is the BCG in the Abell cluster A3816 (Lloyd & Jones 2002).

The count rate for eight of our X-ray detections is higher than 10^{-2} counts s^{-1} ; two of these, MRC B1413–364 and MRC B1737–609, are also found in the Swift-BAT catalogs of hard X-ray sources. For these eight sources, and also for MRC B1346–391, which is close to this rate level, the statistics allowed us to perform a more detailed analysis, investigating the extent of the X-ray emission, the hardness ratio, and the properties of the spectrum in the 0.3–10 keV band.

In addition to PKS B2148–555, we find evidence of deviation from a point-like emission for MRC B0743–673 and MRC B1346–391.

The HR values of MRC B1358–493 and MRC B1413–364 show that their spectrum in the 0.3–10 keV band is hard; note that MRC B1413–364 is one of the two sources included in the Swift-BAT catalogs. The results of the spectral analysis show that a fit with a power law, fixing the hydrogen column density n_H to the Galactic value, adequately describes the spectrum for the investigated sources. However, for MRC B1413–364, an improvement in the fit results after leaving n_H free to vary is found. We consider this improvement as the sign of intrinsic absorption in the lower energy range of the 0.3–10 keV band.

We matched the 20 X-ray detections with infrared and optical catalogs and required a detection in both the in-

frared and the optical bands to establish a counterpart at lower frequencies for our X-ray detections. Based on the analysis of the available information, we rank the 20 SMS4 sources with an XRT detection according to the reliability of the candidate counterpart and establish 18 class A and two class B sources. Class A sources have reliable unique candidates; two class B sources (MRC B0420–625 and MRC B0534–497) each have two possible candidates and thus need further investigation to determine the correct counterpart.

Comparing our results with the counterparts previously proposed by W20 and BH06 for class A sources, our analysis confirms all 12 infrared counterparts provided by W20 and 13 of the 20 optical counterparts provided by BH06. Thus, we associate new infrared counterparts for six sources and five optical alternatives to BH06:

- For MRC B0013–634, MRC B0049–433, MRC B0157–311, MRC B0219–706, MRC B0453–301, MRC B0547–408, MRC B0842–754, and MRC B1143–483, these infrared and optical counterparts match each other.
- For MRC B0007–446, MRC B1413–364, MRC B1451–364, and MRC B1737–609, our analysis supports the infrared identifications proposed by W20. For three of these (MRC B0007–446, MRC B1413–364, and MRC B1451–364), we find an optical source, matching the IR counterpart, whose coordinates differ by more than $2''.5$ from the coordinates of the optical counterparts proposed by BH06, but likely refer to the same object. For MRC B1737–609, the optical counterpart proposed by BH06 refers to a completely different object from the counterparts that we give, including the infrared source provided by W20 (see Fig. 2t). BH06 relied on the radio location alone and the extended radio structure for MRC B1737–609 yielded an incorrect location for the radio core, while the Swift X-ray position correctly identified the AGN core.
- For MRC B1358–493, the position given by BH06 lies outside the XRT error circle: our analysis supports a counterpart detected in both AllWISE and GSC 2.3.2, lying in the overlap between the radio and X-ray error regions; in this case, for the first time, we associate an infrared counterpart with this radio source.
- For MRC B0743–673, MRC B0906–682, MRC B1030–340, MRC B1346–391, and MRC B1445–468, not only we do confirm the

optical counterparts given by BH06, but we also find for them a matching infrared source in WISE catalogs, providing in this way an infrared counterpart also for these five radio sources for the first time.

In conclusion, 18 class A SMS4 sources have candidates detected in both the infrared and optical bands, listed in Table 7, supporting the multifrequency emission that is expected to characterize quasars and radio galaxies that constitute our sample. Nine infrared objects, corresponding to our candidate counterparts, had already been included in the sample of ≈ 1.4 million AGNs assembled by Secrest et al. (2015); three additional sources were found in the Edelson & Malkan (2012) and in the Souchay et al. (2019) samples, for a total of 12 sources.

The results that we have described fill a gap in our knowledge of the X-ray view of powerful radio sources in the Southern Hemisphere, and identify the most promising sources to be investigated further with narrow-field imaging X-ray instruments. Since 2015, when we compiled the list of 45 sources not yet observed by current X-ray observatories with high spatial resolution, excluding the 24 sources for which we obtained Swift observations, only one source, MRC B1706–606, has been observed by Chandra, in 2020.

We provide in the Appendix A (Table 8) the list of the remaining 56 SMS4 sources that in 2021 September still lacked Chandra, Swift, or XMM-Newton observations. After sorting this list by \bar{S}_{181} , in 2021 October we successfully proposed Swift observations for the 18 brightest radio sources. Their \bar{S}_{181} values are in any case higher than 10.9 Jy and vary in the range between 12.7 Jy (MRC B2140–817) and 34.6 Jy (MRC B1526–423).

The authors are grateful to the referee for constructive comments that helped them to expand their analysis, substantially improving and enriching the paper content. They acknowledge Francesco Massaro for sowing the seed aiming at the coverage of the whole SMS4 sample in the X-rays with Swift. They thank Andy Goulding for assistance in understanding the IR emission of AGN and for introducing them to the intricacies of the WISE source catalogs. They also thank the Swift PI, Brad Cenko, and his deputies for approving the requested ToO observations, and the Science Operations Team for implementing them. A.M. thanks Riccardo Campana and Dario Gasparri for their help and support, when needed. A.M. acknowledges financial support from the ASI-INAF agreement No. 2014-049-R0 and its No. 2014-049-R1-2016 and No. 2014-049-R2-2017 addenda. W.F., C.J., and R.K. acknowledge support from the Smithsonian Institution and the Chandra High Resolution Camera Project through NASA contract NAS8-03060. This research has made use of archival data, software, or online services provided by the ASI Space Science Data Center (SSDC); the High Energy Astrophysics Science Archive Research Center (HEASARC) provided by NASA’s Goddard Space Flight Center; the SIMBAD database operated at CDS, Strasbourg, France; the NASA/IPAC Extragalactic Database (NED) operated by the Jet Propulsion Laboratory, California Institute of Technology, under contract with the National Aeronautics and Space Administration; and the NASA/IPAC Infrared Science Archive, which is funded by the National Aeronautics and Space Administration and operated by the California Institute of Technology.

Facilities: Swift (XRT), SkyView Virtual Observatory (<https://skyview.gsfc.nasa.gov/current/cgi/query.pl>), IRSA

Software: HEASoft (Nasa High Energy Astrophysics Science Archive Research Center (Heasarc) 2014), TOPCAT (Taylor 2005), SAO Image DS9 (Smithsonian Astrophysical Observatory 2000; Joye & Mandel 2003)

APPENDIX

A. LIST OF SOURCES NOT YET OBSERVED BY NARROW-FIELD X-RAY INSTRUMENTS

In Table 8, we list the SMS4 sources that had not been observed with any narrow-field telescope (Swift, Chandra, or XMM-Newton) to allow a precise X-ray location as of 2021 October. Since the compilation, we have successfully proposed Swift observations for the 18 brightest sources. These sources are marked in bold.

Table 8. SMS4 Sources with No Data (2021 September) from Narrow-field X-Ray Telescopes on board Swift, Chandra, or XMM-Newton

(1) SMS4 Name	(2) R.A.(J2000) (<i>h m s</i>)	(3) Decl.(J2000) (<i>° ′ ″</i>)	(4) Redshift	(5) S_{178} (Jy)	(6) \bar{S}_{181} (Jy)	(7) LAS (arcsec)	(8) Radio Structure	(9) Optical Counterpart
MRC B0003–833	00 06 14.60	–83 06 00.0	(0.32)	13.2	10.6	60		g
MRC B0036–392	00 38 26.89	–38 59 46.7	0.592	12.7	9.5	10	D2	Q
MRC B0103–453	01 05 20.88	–45 05 28.2	(0.71)	19.0	17.6	140		g d
MRC B0110–692	01 11 42.88	–68 59 59.3	(>0.56)	12.2	10.0	56		BF
MRC B0119–634	01 21 40.36	–63 09 02.0	0.837	11.4	9.1	43	2	Q
MRC B0202–765	02 02 13.53	–76 20 06.8	0.38925	19.0	14.9	20	2	Q
MRC B0242–514	02 43 44.56	–51 12 36.7	(0.72)	19.0	13.6	53	2	g d
MRC B0251–675	02 51 56.30	–67 18 02.6	1.002	13.5	8.6	38	2	Q
PKS B0319–45	03 21 08.10	–45 12 51.0	0.0633	13.5	14.5	1536		g
MRC B0344–345	03 46 31.10	–34 22 40.0	0.0538	18.0	14.6	264		g
MRC B0427–366	04 29 40.17	–36 30 55.2		18.0	14.7	14	2	Q?
MRC B0456–301	04 58 26.43	–30 07 22.4	0.063	13.3	11.1	348		g
MRC B0511–484	05 12 50.79	–48 24 04.3	0.30638	12.2	14.4	132		g
PKS B0511–30	05 13 34.60	–30 28 24.0	0.0583	16.0	13.2	636		g
MRC B0646–398	06 48 11.30	–39 57 07.3		13.9	11.0	82		Q?
MRC B0658–656	06 58 12.84	–65 44 53.3	(>0.14)	11.0	9.8	25	2	O
MRC B0719–553	07 20 14.63	–55 25 16.4	0.216	11.9	8.9	52		g
MRC B1017–426	10 20 03.77	–42 51 31.5	1.28	23.0	21.3	10	2	Q
MRC B1123–351	11 25 54.46	–35 23 19.7	0.032	11.3	9.9	60		g
MRC B1136–320	11 39 17.17	–32 22 33.2	(0.67)	14.0	12.0	62		g d
MRC B1143–316	11 46 20.55	–31 57 14.5	(1.35)	12.7	9.5	46		g d
MRC B1215–457	12 18 06.23	–46 00 28.6	0.529	12.8	12.4	10	c	Q
MRC B1421–382	14 24 16.53	–38 26 49.9	0.4068	15.0	12.5	61	2	Q
MRC B1425–479	14 28 57.20	–48 12 02.0	(0.11)	13.0	12.2	270		g
MRC B1526–423	15 30 14.30	–42 31 53.2	(0.5)	44.0	34.6	50	2	g d
MRC B1607–841	16 19 34.05	–84 18 18.9	(1.11)	11.2	7.1	10	c	g e
MRC B1716–800	17 25 25.68	–80 04 45.4	(0.45)	12.7	10.8	43		g
MRC B1721–836	17 33 55.37	–83 42 53.3	(1.42)	13.0	5.5	10	2	g
MRC B1754–597	17 59 06.31	–59 46 59.6	(0.8)	20.0	25.2	21	2	g
MRC B1756–663	18 01 17.96	–66 23 02.9	(0.93)	11.6	8.5	10	c	g
MRC B1814–519	18 18 06.96	–51 58 09.6	(0.48)	24.0	23.5	10	2	g
MRC B1817–391	18 20 35.31	–39 09 28.4	(0.91)	19.0	15.7	16	2	g d
MRC B1817–640	18 22 16.10	–63 59 19.3	0.67	28.0	21.4	31	2	g
MRC B1827–360	18 30 58.90	–36 02 30.3	(0.12)	33.0	30.1	10	c	g
MRC B1840–404	18 44 28.35	–40 21 55.8	(1.77)	16.0	14.4	46		g d
MRC B1933–587	19 37 32.37	–58 38 27.8	1.92	14.0	14.1	10	T	Q
MRC B1940–406	19 43 51.87	–40 30 10.2	(0.18)	14.0	11.5	126		g
MRC B1953–425	19 57 15.22	–42 22 20.1	(0.82)	18.0	15.9	10	c	g
MRC B2032–350	20 35 47.66	–34 54 02.5	(0.56)	27.0	23.9	26	2	g d
MRC B2041–604	20 45 20.72	–60 19 01.3	1.464	27.0	20.8	32		g
MRC B2049–368	20 52 17.50	–36 40 29.8	(0.89)	11.4	9.5	10	2	g
MRC B2115–305	21 18 10.68	–30 19 14.7	0.98	11.4	10.5	12	2	Q
MRC B2140–434	21 43 33.46	–43 12 48.5	0.65	19.0	14.7	56	2	Q
MRC B2140–817	21 47 23.96	–81 32 11.7	(0.64)	26.0	12.7	44	2	g
MRC B2150–520	21 54 07.47	–51 50 15.0	(0.79)	18.0	15.1	15	2	g
MRC B2201–555	22 05 04.89	–55 17 43.3	(0.51)	13.1	8.9	10	2	g
MRC B2223–528	22 27 02.69	–52 33 25.4	(0.41)	17.0	13.7	11	2	g
MRC B2226–411	22 29 18.47	–40 51 31.7	0.4462	11.3	9.3	15	T	Q
MRC B2226–386	22 29 46.90	–38 23 59.2	(1.3)	14.0	11.5	10	2	g
MRC B2252–530	22 55 50.13	–52 45 42.4	(0.55)	12.1	7.9	10	2	g
MRC B2253–522	22 56 47.53	–51 58 41.5	(0.43)	15.0	10.2	11	2	g d
MRC B2259–375	23 02 23.86	–37 18 05.8	(1.14)	13.0	10.0	10		g
MRC B2323–407	23 26 34.12	–40 27 17.8	(0.81)	15.0	11.9	10	2	g
MRC B2331–416	23 34 26.13	–41 25 25.1	0.907	30.0	23.7	19	2	g
MRC B2332–668	23 35 11.29	–66 37 04.6	(0.08)	12.7	9.7	28	2	O
MRC B2338–585	23 41 18.36	–58 16 10.3	(0.64)	15.0	11.8	10	2	g d

NOTE—Column (1): the name in SMS4, according to the MRC or PKS designation, with bold characters to mark those accepted in 2021 October for observation with Swift. Columns (2) and (3): R.A. and decl. of the SMS4 source. Column (4): the redshift, with lower limits and photometric estimates in parentheses. Column (5): the extrapolated flux density S_{178} from SMS4. Column (6): the total integrated flux density \bar{S}_{181} from G4Jy. Column (7): the largest angular size of the radio source at 843 MHz. Column (8): the structural classification of the radio source, following Fanaroff & Riley (1974), where 2 = FR2 double; D2 = double, with one component coincident with the optical counterpart; T = core-dominated triple; c = structure not resolved well enough to classify. Column (9): the classification of the associated optical counterpart, where d = extended radio source with more than one candidate; e = compact radio source with large radio-optical offset; g = galaxy; Q = quasar; Q? = quasar candidate; BF = blank field; O = field obscured by star.

REFERENCES

- Abbott, T. M. C., Adamów, M., Agüena, M., et al. 2021, *ApJS*, 255, 20, doi: [10.3847/1538-4365/ac00b3](https://doi.org/10.3847/1538-4365/ac00b3)
- Barthelmy, S. D., Barbier, L. M., Cummings, J. R., et al. 2005, *SSRv*, 120, 143, doi: [10.1007/s11214-005-5096-3](https://doi.org/10.1007/s11214-005-5096-3)
- Bennett, A. S. 1962, *MmRAS*, 68, 163
- Burgess, A. M., & Hunstead, R. W. 2006a, *AJ*, 131, 100, doi: [10.1086/498677](https://doi.org/10.1086/498677)
- . 2006b, *AJ*, 131, 114, doi: [10.1086/498679](https://doi.org/10.1086/498679)
- Burrows, D. N., Hill, J. E., Nousek, J. A., et al. 2005, *SSRv*, 120, 165, doi: [10.1007/s11214-005-5097-2](https://doi.org/10.1007/s11214-005-5097-2)
- Bykov, A. M., Churazov, E. M., Ferrari, C., et al. 2015, *SSRv*, 188, 141, doi: [10.1007/s11214-014-0129-4](https://doi.org/10.1007/s11214-014-0129-4)
- Churazov, E., Sazonov, S., Sunyaev, R., et al. 2005, *MNRAS*, 363, L91, doi: [10.1111/j.1745-3933.2005.00093.x](https://doi.org/10.1111/j.1745-3933.2005.00093.x)
- Churazov, E., Sunyaev, R., Forman, W., & Böhringer, H. 2002, *MNRAS*, 332, 729, doi: [10.1046/j.1365-8711.2002.05332.x](https://doi.org/10.1046/j.1365-8711.2002.05332.x)
- Condon, J. J., Cotton, W. D., Greisen, E. W., et al. 1998, *AJ*, 115, 1693, doi: [10.1086/300337](https://doi.org/10.1086/300337)
- Crain, R. A., Schaye, J., Bower, R. G., et al. 2015, *MNRAS*, 450, 1937, doi: [10.1093/mnras/stv725](https://doi.org/10.1093/mnras/stv725)
- Croton, D. J., Springel, V., White, S. D. M., et al. 2006, *MNRAS*, 365, 11, doi: [10.1111/j.1365-2966.2005.09675.x](https://doi.org/10.1111/j.1365-2966.2005.09675.x)
- Croton, D. J., Stevens, A. R. H., Tonini, C., et al. 2016, *ApJS*, 222, 22, doi: [10.3847/0067-0049/222/2/22](https://doi.org/10.3847/0067-0049/222/2/22)
- Cutri, R. M., Wright, E. L., Conrow, T., et al. 2013, Explanatory Supplement to the AllWISE Data Release Products, Explanatory Supplement to the AllWISE Data Release Products, by R. M. Cutri et al.
- . 2014, *VizieR Online Data Catalog*, II/328
- Dasadia, S., Sun, M., Morandi, A., et al. 2016, *MNRAS*, 458, 681, doi: [10.1093/mnras/stw291](https://doi.org/10.1093/mnras/stw291)
- Dunkley, J., Komatsu, E., Nolta, M. R., et al. 2009, *ApJS*, 180, 306, doi: [10.1088/0067-0049/180/2/306](https://doi.org/10.1088/0067-0049/180/2/306)
- Edelson, R., & Malkan, M. 2012, *ApJ*, 751, 52, doi: [10.1088/0004-637X/751/1/52](https://doi.org/10.1088/0004-637X/751/1/52)
- Edge, D. O., Shakeshaft, J. R., McAdam, W. B., Baldwin, J. E., & Archer, S. 1959, *MmRAS*, 68, 37
- Evans, P. A., Page, K. L., Osborne, J. P., et al. 2020, *ApJS*, 247, 54, doi: [10.3847/1538-4365/ab7db9](https://doi.org/10.3847/1538-4365/ab7db9)
- Fabian, A. C. 1994, *ARA&A*, 32, 277, doi: [10.1146/annurev.aa.32.090194.001425](https://doi.org/10.1146/annurev.aa.32.090194.001425)
- Fanaroff, B. L., & Riley, J. M. 1974, *MNRAS*, 167, 31P, doi: [10.1093/mnras/167.1.31P](https://doi.org/10.1093/mnras/167.1.31P)
- Finoguenov, A., & Jones, C. 2001, *ApJL*, 547, L107, doi: [10.1086/318910](https://doi.org/10.1086/318910)
- Forman, W., Jones, C., & Tucker, W. 1985, *ApJ*, 293, 102, doi: [10.1086/163218](https://doi.org/10.1086/163218)
- Forman, W., Nulsen, P., Heinz, S., et al. 2005, *ApJ*, 635, 894, doi: [10.1086/429746](https://doi.org/10.1086/429746)
- Forman, W., Jones, C., Churazov, E., et al. 2007, *ApJ*, 665, 1057, doi: [10.1086/519480](https://doi.org/10.1086/519480)
- Gehrels, N., Chincarini, G., Giommi, P., et al. 2004, *ApJ*, 611, 1005, doi: [10.1086/422091](https://doi.org/10.1086/422091)
- Gilli, R. 2004, *Advances in Space Research*, 34, 2470, doi: [10.1016/j.asr.2003.03.073](https://doi.org/10.1016/j.asr.2003.03.073)
- Hardcastle, M. J., Massaro, F., & Harris, D. E. 2010, *MNRAS*, 401, 2697, doi: [10.1111/j.1365-2966.2009.15855.x](https://doi.org/10.1111/j.1365-2966.2009.15855.x)
- HI4PI Collaboration, Ben Bekhti, N., Flöer, L., et al. 2016, *A&A*, 594, A116, doi: [10.1051/0004-6361/201629178](https://doi.org/10.1051/0004-6361/201629178)
- Hurley-Walker, N., Callingham, J. R., Hancock, P. J., et al. 2017, *MNRAS*, 464, 1146, doi: [10.1093/mnras/stw2337](https://doi.org/10.1093/mnras/stw2337)
- Intema, H. T., Jagannathan, P., Mooley, K. P., & Frail, D. A. 2017, *A&A*, 598, A78, doi: [10.1051/0004-6361/201628536](https://doi.org/10.1051/0004-6361/201628536)
- Jacobs, D. C., Aguirre, J. E., Parsons, A. R., et al. 2011, *ApJL*, 734, L34, doi: [10.1088/2041-8205/734/2/L34](https://doi.org/10.1088/2041-8205/734/2/L34)
- Jimenez-Gallardo, A., Massaro, F., Prieto, M. A., et al. 2020, *ApJS*, 250, 7, doi: [10.3847/1538-4365/aba5a0](https://doi.org/10.3847/1538-4365/aba5a0)
- Jones, C., Forman, W., Vikhlinin, A., et al. 2002, *ApJL*, 567, L115, doi: [10.1086/340114](https://doi.org/10.1086/340114)
- Jones, P. A., & McAdam, W. B. 1992, *ApJS*, 80, 137, doi: [10.1086/191662](https://doi.org/10.1086/191662)
- Joye, W. A., & Mandel, E. 2003, in *Astronomical Society of the Pacific Conference Series*, Vol. 295, *Astronomical Data Analysis Software and Systems XII*, ed. H. E. Payne, R. I. Jedrzejewski, & R. N. Hook, 489
- Kraft, R. P., Vázquez, S. E., Forman, W. R., et al. 2003, *ApJ*, 592, 129, doi: [10.1086/375533](https://doi.org/10.1086/375533)
- Laing, R. A., Riley, J. M., & Longair, M. S. 1983, *MNRAS*, 204, 151, doi: [10.1093/mnras/204.1.151](https://doi.org/10.1093/mnras/204.1.151)
- Large, M. I., Cram, L. E., & Burgess, A. M. 1991, *The Observatory*, 111, 72
- Large, M. I., Mills, B. Y., Little, A. G., Crawford, D. F., & Sutton, J. M. 1981, *MNRAS*, 194, 693, doi: [10.1093/mnras/194.3.693](https://doi.org/10.1093/mnras/194.3.693)
- Lasker, B. M., Lattanzi, M. G., McLean, B. J., et al. 2008, *AJ*, 136, 735, doi: [10.1088/0004-6256/136/2/735](https://doi.org/10.1088/0004-6256/136/2/735)
- Lloyd, B. D., & Jones, P. A. 2002, *MNRAS*, 331, 717, doi: [10.1046/j.1365-8711.2002.05239.x](https://doi.org/10.1046/j.1365-8711.2002.05239.x)
- Lovisari, L., Reiprich, T. H., & Schellenberger, G. 2015, *A&A*, 573, A118, doi: [10.1051/0004-6361/201423954](https://doi.org/10.1051/0004-6361/201423954)
- Madrid, J. P., Donzelli, C. J., Rodríguez-Ardila, A., et al. 2018, *ApJS*, 238, 31, doi: [10.3847/1538-4365/aade8f](https://doi.org/10.3847/1538-4365/aade8f)
- Marocco, F., Eisenhardt, P. R. M., Fowler, J. W., et al. 2021, *ApJS*, 253, 8, doi: [10.3847/1538-4365/abd805](https://doi.org/10.3847/1538-4365/abd805)

- Maselli, A., Kraft, R. P., Massaro, F., & Hardcastle, M. J. 2018, *A&A*, 619, A75, doi: [10.1051/0004-6361/201833332](https://doi.org/10.1051/0004-6361/201833332)
- Maselli, A., Massaro, F., Cusumano, G., et al. 2013, *ApJS*, 206, 17, doi: [10.1088/0067-0049/206/2/17](https://doi.org/10.1088/0067-0049/206/2/17)
- . 2016, *MNRAS*, 460, 3829, doi: [10.1093/mnras/stw1222](https://doi.org/10.1093/mnras/stw1222)
- Massaro, E., Giommi, P., Leto, C., et al. 2009a, *A&A*, 495, 691, doi: [10.1051/0004-6361:200810161](https://doi.org/10.1051/0004-6361:200810161)
- Massaro, F., Harris, D. E., Tremblay, G. R., et al. 2013, *ApJS*, 206, 7, doi: [10.1088/0067-0049/206/1/7](https://doi.org/10.1088/0067-0049/206/1/7)
- Massaro, F., Chiaberge, M., Grandi, P., et al. 2009b, *ApJL*, 692, L123, doi: [10.1088/0004-637X/692/2/L123](https://doi.org/10.1088/0004-637X/692/2/L123)
- Massaro, F., Harris, D. E., Tremblay, G. R., et al. 2010, *ApJ*, 714, 589, doi: [10.1088/0004-637X/714/1/589](https://doi.org/10.1088/0004-637X/714/1/589)
- Massaro, F., Tremblay, G. R., Harris, D. E., et al. 2012, *ApJS*, 203, 31, doi: [10.1088/0067-0049/203/2/31](https://doi.org/10.1088/0067-0049/203/2/31)
- Massaro, F., Harris, D. E., Liuzzo, E., et al. 2015, *ApJS*, 220, 5, doi: [10.1088/0067-0049/220/1/5](https://doi.org/10.1088/0067-0049/220/1/5)
- Massaro, F., Missaglia, V., Stuardi, C., et al. 2018, *ApJS*, 234, 7, doi: [10.3847/1538-4365/aa8e9d](https://doi.org/10.3847/1538-4365/aa8e9d)
- Mauch, T., Murphy, T., Buttery, H. J., et al. 2003, *MNRAS*, 342, 1117, doi: [10.1046/j.1365-8711.2003.06605.x](https://doi.org/10.1046/j.1365-8711.2003.06605.x)
- McNamara, B. R., & Nulsen, P. E. J. 2007, *ARA&A*, 45, 117, doi: [10.1146/annurev.astro.45.051806.110625](https://doi.org/10.1146/annurev.astro.45.051806.110625)
- . 2012, *New Journal of Physics*, 14, 055023, doi: [10.1088/1367-2630/14/5/055023](https://doi.org/10.1088/1367-2630/14/5/055023)
- Missaglia, V., Massaro, F., Liuzzo, E., et al. 2021, *ApJS*, 255, 18, doi: [10.3847/1538-4365/ac00b6](https://doi.org/10.3847/1538-4365/ac00b6)
- Moretti, A., Campana, S., Mineo, T., et al. 2005, in *Society of Photo-Optical Instrumentation Engineers (SPIE) Conference Series*, Vol. 5898, UV, X-Ray, and Gamma-Ray Space Instrumentation for Astronomy XIV, ed. O. H. W. Siegmund, 360–368
- Nasa High Energy Astrophysics Science Archive Research Center (Heasarc). 2014, HEASoft: Unified Release of FTOOLS and XANADU. <http://ascl.net/1408.004>
- Pillepich, A., Springel, V., Nelson, D., et al. 2018, *MNRAS*, 473, 4077, doi: [10.1093/mnras/stx2656](https://doi.org/10.1093/mnras/stx2656)
- Randall, S. W., Forman, W. R., Giacintucci, S., et al. 2011, *ApJ*, 726, 86, doi: [10.1088/0004-637X/726/2/86](https://doi.org/10.1088/0004-637X/726/2/86)
- Randall, S. W., Nulsen, P. E. J., Jones, C., et al. 2015, *ApJ*, 805, 112, doi: [10.1088/0004-637X/805/2/112](https://doi.org/10.1088/0004-637X/805/2/112)
- Rojas, A. F., Masetti, N., Minniti, D., et al. 2017, *A&A*, 602, A124, doi: [10.1051/0004-6361/201629463](https://doi.org/10.1051/0004-6361/201629463)
- Sadler, E. M., Ricci, R., Ekers, R. D., et al. 2006, *MNRAS*, 371, 898, doi: [10.1111/j.1365-2966.2006.10729.x](https://doi.org/10.1111/j.1365-2966.2006.10729.x)
- Schaye, J., Crain, R. A., Bower, R. G., et al. 2015, *MNRAS*, 446, 521, doi: [10.1093/mnras/stu2058](https://doi.org/10.1093/mnras/stu2058)
- Secrest, N. J., Dudik, R. P., Dorland, B. N., et al. 2015, *ApJS*, 221, 12, doi: [10.1088/0067-0049/221/1/12](https://doi.org/10.1088/0067-0049/221/1/12)
- Segreto, A., Cusumano, G., Ferrigno, C., et al. 2010, *A&A*, 510, A47, doi: [10.1051/0004-6361/200911779](https://doi.org/10.1051/0004-6361/200911779)
- Simpson, C., Clements, D. L., Rawlings, S., & Ward, M. 1993, *MNRAS*, 262, 889, doi: [10.1093/mnras/262.4.889](https://doi.org/10.1093/mnras/262.4.889)
- Slee, O. B. 1995, *Australian Journal of Physics*, 48, 143, doi: [10.1071/PH950143](https://doi.org/10.1071/PH950143)
- Smithsonian Astrophysical Observatory. 2000, SAOImage DS9: A utility for displaying astronomical images in the X11 window environment. <http://ascl.net/0003.002>
- Souchay, J., Gattano, C., Andrei, A. H., et al. 2019, *A&A*, 624, A145, doi: [10.1051/0004-6361/201834955](https://doi.org/10.1051/0004-6361/201834955)
- Stern, D., Assef, R. J., Benford, D. J., et al. 2012, *ApJ*, 753, 30, doi: [10.1088/0004-637X/753/1/30](https://doi.org/10.1088/0004-637X/753/1/30)
- Stuardi, C., Missaglia, V., Massaro, F., et al. 2018, *ApJS*, 235, 32, doi: [10.3847/1538-4365/aaafcf](https://doi.org/10.3847/1538-4365/aaafcf)
- Taylor, M. B. 2005, in *Astronomical Society of the Pacific Conference Series*, Vol. 347, *Astronomical Data Analysis Software and Systems XIV*, ed. P. Shopbell, M. Britton, & R. Ebert, 29
- Tingay, S. J., Goeke, R., Bowman, J. D., et al. 2013, *PASA*, 30, e007, doi: [10.1017/pasa.2012.007](https://doi.org/10.1017/pasa.2012.007)
- Tohuvavohu, A., Evans, P., Kennea, J., & Cenko, S. B. 2019, in *American Astronomical Society Meeting Abstracts*, Vol. 233, *American Astronomical Society Meeting Abstracts #233*, 210.08
- Tueller, J., Baumgartner, W. H., Markwardt, C. B., et al. 2010, *ApJS*, 186, 378, doi: [10.1088/0067-0049/186/2/378](https://doi.org/10.1088/0067-0049/186/2/378)
- Vogelsberger, M., Genel, S., Sijacki, D., et al. 2013, *MNRAS*, 436, 3031, doi: [10.1093/mnras/stt1789](https://doi.org/10.1093/mnras/stt1789)
- Wayth, R. B., Lenc, E., Bell, M. E., et al. 2015, *PASA*, 32, e025, doi: [10.1017/pasa.2015.26](https://doi.org/10.1017/pasa.2015.26)
- Werner, N., McNamara, B. R., Churazov, E., & Scannapieco, E. 2019, *SSRv*, 215, 5, doi: [10.1007/s11214-018-0571-9](https://doi.org/10.1007/s11214-018-0571-9)
- White, S. V., Franzen, T. M. O., Riseley, C. J., et al. 2020a, *PASA*, 37, e018, doi: [10.1017/pasa.2020.9](https://doi.org/10.1017/pasa.2020.9)
- . 2020b, *PASA*, 37, e017, doi: [10.1017/pasa.2020.10](https://doi.org/10.1017/pasa.2020.10)